Biophysical Journal
Article

Biophysical Society

Activation mechanism of the human Smoothened receptor

Prateek D. Bansal,[1] Soumajit Dutta,[1] and Diwakar Shukla[1,2,3,4,*]
[1]Department of Chemical and Biomolecular Engineering, University of Illinois at Urbana-Champaign, Urbana, Illinois; [2]Department of Bioengineering, University of Illinois at Urbana-Champaign, Urbana, Illinois; [3]Center for Biophysics and Quantitative Biology, University of Illinois at Urbana-Champaign, Urbana, Illinois; and [4]Cancer Center at Illinois, University of Illinois at Urbana-Champaign, Urbana, Illinois

ABSTRACT Smoothened (SMO) is a membrane protein of the class F subfamily of G protein-coupled receptors (GPCRs) and maintains homeostasis of cellular differentiation. SMO undergoes conformational change during activation, transmitting the signal across the membrane, making it amenable to bind to its intracellular signaling partner. Receptor activation has been studied at length for class A receptors, but the mechanism of class F receptor activation remains unknown. Agonists and antagonists bound to SMO at sites in the transmembrane domain (TMD) and the cysteine-rich domain have been characterized, giving a static view of the various conformations SMO adopts. Although the structures of the inactive and active SMO outline the residue-level transitions, a kinetic view of the overall activation process remains unexplored for class F receptors. We describe SMO's activation process in atomistic detail by performing 300 μs of molecular dynamics simulations and combining it with Markov state model theory. A molecular switch, conserved across class F and analogous to the activation-mediating D-R-Y motif in class A receptors, is observed to break during activation. We also show that this transition occurs in a stage-wise movement of the transmembrane helices: TM6 first, followed by TM5. To see how modulators affect SMO activity, we simulated agonist and antagonist-bound SMO. We observed that agonist-bound SMO has an expanded hydrophobic tunnel in SMO's core TMD, whereas antagonist-bound SMO shrinks this tunnel, further supporting the hypothesis that cholesterol travels through a tunnel inside Smoothened to activate it. In summary, this study elucidates the distinct activation mechanism of class F GPCRs and shows that SMO's activation process rearranges the core TMD to open a hydrophobic conduit for cholesterol transport.

SIGNIFICANCE Hedgehog signaling via the Smoothened receptor is critical for maintaining homeostasis of cellular differentiation. Smoothened antagonists have been designed to treat basal cell carcinoma and pediatric medulloblastoma. Signaling via SMO involves an equilibrium between its inactive and active states, and hence studying the dynamics of Smoothened activation is critical to design chemotherapeutics. Here we use molecular dynamics simulations to construct a statistical Markov state model that gives us a way to characterize the conformational transitions of Smoothened from an inactive to active state. We show that Smoothened's activation involves a conserved network motif that is broken on activation. Upon agonist binding, we observe that a hydrophobic tunnel inside Smoothened's transmembrane domain opens in the upper leaflet.

INTRODUCTION

G protein-coupled receptors (GPCRs) act as molecular telephones and transmit signals across the cellular membrane by associating with G proteins (1,2) or arrestins (3). The process of signal transduction generally involves GPCRs binding to agonists that aid the shift in conformational equilibrium, facilitating the receptors to transition to an active state. Activation allows the receptor to associate with intracellular binding partners, allowing the process of signal transduction (4). GPCR activation is an area of active research, with studies establishing conserved structural motifs such as the E/DRY, NPxxY (4–8) in class A, and PxxG and HETx (9) in class B receptors acting as molecular switches that stabilize the inactive state. Unlike class A and B GPCRs, activation of class F receptors Smoothened (SMO) and Frizzleds1-10 (FZD_{1-10}) is still poorly understood. A primary reason for this elusiveness is that these receptors share none of the structural motifs seen in class A/B, and have less than 10% sequence similarity to class A receptors (10) as well as class B receptors. Since class A and B GPCRs are involved in mediating virtually every

Submitted August 5, 2022, and accepted for publication March 2, 2023.
*Correspondence: diwakar@illinois.edu
Editor: Alan Grossfield.
https://doi.org/10.1016/j.bpj.2023.03.007

physiological response, they are crucial drug targets, as 34% of all US Food and Drug Administration (FDA)-approved drugs target one of these proteins (11).

SMO is a transmembrane protein from the class F of GPCRs. Class F consists of proteins that are involved in maintaining tissue homeostasis and regenerative responses in adults, and are crucial in embryonic development, as they regulate cellular differentiation by binding to sterol and Wnt ligands (12–15). SMO is expressed in tissues throughout the body, particularly in cerebellar and pituitary tissue (16), and is a member of the Hedgehog (HH) signaling pathway. When the endogenous inhibitor of SMO, a membrane protein Patched (PTCH), is inhibited by Sonic Hedgehog (Shh) binding, SMO translocates to the ciliary membrane and undergoes conformational transitions (activation) to bind to its intracellular signaling partner G_i (17,18). How PTCH inhibits SMO is still unclear. However, multiple studies have described PTCH's inhibition on SMO as acting through reducing SMO's accessibility to membrane cholesterol (19). A recent study described the effect of PTCH on the cholesterol accessibility of the upper leaflet, suggesting that PTCH inhibits SMO by transporting cholesterol either to the inner leaflet or to an extracellular acceptor (20). HH signaling is critical to embryonic development, and any changes in signaling can lead to severe birth defects (21). Cyclopamine, a naturally occurring alkaloid in corn lily, has been identified as a teratogen (agents responsible for birth defects in infants) (22), and was responsible for birth defects in lambs in Idaho in the 1950s (23). It was identified later that cyclopamine's mechanism of action involved inhibiting HH signaling by binding to SMO (24–26). On the other hand, overstimulation of HH signaling via SMO has been linked to the pathogenesis of pediatric medulloblastoma and basal cell carcinoma (27,28). Vismodegib (29) and sonidegib (30) are two FDA-approved drugs that target SMO but are prone to chemoresistance (31). Therefore, understanding activation mechanisms of class F GPCRs is critical to the design of novel therapeutics.

Structures of SMO bound to agonists and antagonists outline the effects of allosteric and orthosteric modulator binding on SMO activity. These structures show the existence of two primary binding sites in SMO, the first in the cysteine-rich domain (CRD), which binds agonists cholesterol (32) and cyclopamine (33). The second site is present in the transmembrane domain (TMD), which binds both antagonists LY2940680 (10), SANT1 and AntaXV (34), cyclopamine (35), TC114 (36), and vismodegib (32) and agonists SAG1.5 (34), SAG (37), SAG21k (38), 24,25-epoxycholesterol (39), and cholesterol (37). Mutagenesis studies have outlined the presence of an intracellular $W^{7.55f}$-$R^{6.32f}$ π-cation lock(40) in class F that is broken on activation (Fig. 1 *A*), with mutations that disrupt this lock leading to increased agonist potency and pathway selection (superscripts refer to the modified Ballesteros-Weinstein numbering system used to denote class F GPCR TM residues (41) introduced by Wang et al. (34)). On the extracellular end, for SAG-bound SMO, the D-R-E network is broken in active SMO (34) (Fig. 1 *A*). The intracellular end of active SMO shows rearrangements in TM6 (outward), TM3 (outward), and TM5 (inward) (Fig. 1 *B*). These studies paint a static picture of how SMO activity can be attributed to structural rearrangements; however, a dynamic understanding of the process of SMO activation still remains. Hence, to provide a dynamic overview of activation, we simulated ~250-μs Apo-SMO (no ligand bound) to understand SMO's activation process in atomistic detail. Moreover, it has been shown that PTCH modulates SMO activity by controlling its access to membrane cholesterol (19,42), which then travels through a hydrophobic tunnel inside SMO to access the primary ligand binding site in CRD, showing an expanded tunnel in active SMO (Fig. 1 *A*). Hence, we simulated agonist-bound (SAG-SMO) (~36 μs) and antagonist-bound (SANT1-SMO) (~ 42 μs) SMO to explore the effects of bound modulators on SMO activity, and the mechanisms of action for these molecules. Using a highly parallel adaptive sampling-based approach and constructing a Markov state model (MSM) (43,44), we probe sub-millisecond dynamics of SMO, and show that SMO activation involves an intracellular structural motif that is conserved across class F receptors. MSMs have been used to model membrane protein behavior at varied timescales, to probe activity of membrane transporters (45–47) as well as to study conformational dynamics of signaling proteins (8,48–55). In particular, MSMs have been employed to investigate conformational dynamics of GPCRs, such as β2-adrenergic receptor (8,52,56), dopamine D_3 receptor (48), μ-opioid receptor (54,55), chemokine receptor CCR2 (49), and cannabinoid receptors 1 and 2 (50,51). Using MSMs, we outline the involvement of multiple CRD–TMD salt bridges that are rearranged during SMO activation, establishing a role for the CRD in SMO activation. We show that the hydrophobic tunnel inside SMO expands in the presence of an agonist and is occluded by the antagonist. These observations are amenable to experimental observations that bolster the cholesterol-transport-like activity of SMO. We then use a mutual-information-based approach to outline the allosteric mechanisms through which the agonist SAG operates; i.e., by changing the allosteric pathways in SMO to more active-like SMO. These observations provide a detailed and atomistic in-depth view of SMO activation and may aid in the design of antagonists for cancer therapy.

METHODS

Molecular dynamics simulations

Simulation setup

SMO structures in the bound inactive conformation (inactive SMO) (PDB: 5L7D (32)) and active conformation (active SMO) (PDB: 6XBL (37))

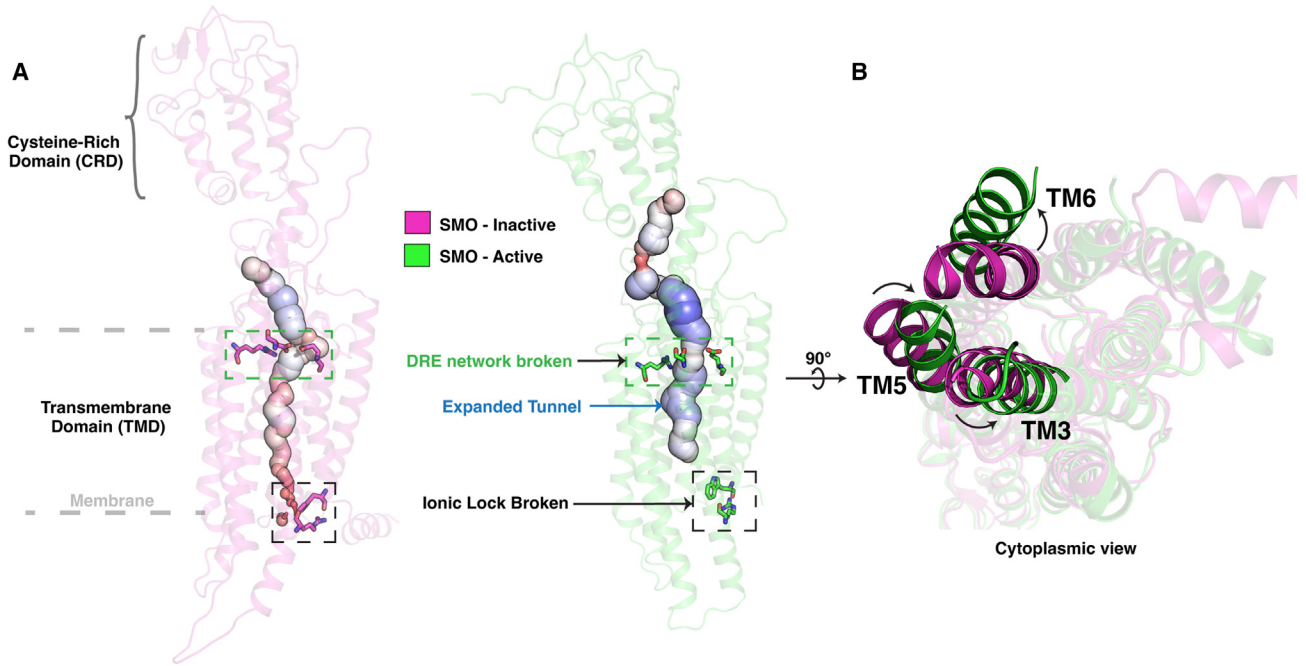

FIGURE 1 Major structural changes during SMO activation. (*A*) Comparison of the broken D-R-E network and the W-R π-cation lock, and the expanded tunnel, in inactive (magenta, 5L7D (32)) vs. active (green, 6XBL (39)) SMO. (*B*) Comparison of inactive and active SMO, indicating the outward movement of the TM6 and TM3 and inward movement of TM5 in active SMO. To see this figure in color, go online.

were used as starting points for the SMO-Apo simulations. For apo systems, the bound ligand and the stabilizing antibodies were removed. The missing residues in the proteins were modeled using MODELLER (57) (Table S3). The inactivating mutation V329F in the inactive SMO was corrected back to wild type. For SAG-SMO, the bound SAG was retained in the SMO-SAG complex (37). To check for the protonations in acidic residues under physiological conditions, the pKa was calculated using the H++ server (58). Accordingly, E518 was protonated in all SMO systems. For SANT1-SMO, owing to the lack of the CRD in the SANT1-SMO complex (PDB: 4N4W (34)), we sought to use the inactive orientation of 5L7D (inactive SMO, CRD present) instead. The SANT1-bound crystal structure (4N4W) was aligned to inactive SMO 5L7D (to maintain the same binding pose for SANT1), and the 5L7D-SANT1 starting point was used for simulations. The terminal residues were capped using neutral terminal caps acetyl (ACE) for N terminus and methylamide (NME) for the C terminus. The proteins were embedded in a membrane bilayer using CHARMM-GUI (59,60). The atomic interactions were characterized using the CHARMM36 force field (61,62). The choice of CHARMM36 force field was based on studies that use CHARMM36 to simulate various GPCRs, specifically at the time of system setup (63–66). Use of CHARMM36m force field made no significant difference to the overall observations (Fig. S1). The force field parameters for synthetic ligands SAG and SANT1 were generated using ParamChem (67), an automated version of CGenFF (68,69). Owing to presence of penalties >10 assigned by CGenFF for various angles and dihedrals for both SAG and SANT1, optimization using the MP2/6-31G* QM calculations was performed. The python-based library Psi4 was used for this purpose (70). Input files were generated using the Web-based input generator CHARMM-GUI (71). The composition of the membrane bilayer was based on lipid composition of the mice brain cerebellum (72) (75% 1-Palmitoyl-2-oleoylphosphatidylcholine (POPC), 21% cholesterol, 4% sphingomyelin) (Table S4), to mimic physiological cerebellar membrane composition. The system was solvated using TIP3P water (73) and 150 mM NaCl, to mimic physiological conditions. Overall the system sizes for inactive SMO, active SMO, SAG-SMO, and SANT1-SMO were 106,415, 105,971, 105,100, and 105,582 atoms, with box sizes 86 × 86 × 153 Å^3, 86 × 86 × 152 Å^3 86 × 86 × 152 Å^3 and 85 × 85 × 153 Å^3 respectively. The mass of non-protein hydrogens was repartitioned to 3.024 Da (74) to enable simulations with a long timestep (4 fs). Parmed, a part of the AmberTools19 package, was used for this purpose (75).

Pre-production MD

The systems were minimized for 1000 steps, using the steepest descent method, followed by minimization using the SHAKE algorithm (76) for 14,000 steps. Systems were then heated from 0 to 310 K using NVT conditions for 5 ns, constraining the backbone using a force constant of 10 kcal mol^{-1} Å^{-2}. Systems were then equilibrated using the NPT conditions for 5 ns, at 310 K and 1 bar, using similar backbone restraints. This was followed by an equilibration of 40 ns, without constraints. Apo-SMO and SANT-SMO simulations were performed using the AMBER18 (75,77–80) biomolecular simulation package. SAG-SMO simulations were performed using NAMD 2.14 (81,82). NAMD was used in this case to aid the simulation of lone pairs associated with the chlorine atom in SAG.

Production MD

Post equilibration, the GPU-accelerated pmemd.cuda package from AMBER18 (75,80) was used for production MD. Integrator timestep was set to 4 fs. Periodic boundary conditions were used, and the temperature was maintained using the Langevin thermostat (83). Pressure of each of the systems was set 1 bar and was maintained using the Monte Carlo barostat. The particle mesh Ewald (84) (PME) method was used for computing long-range electrostatic interactions. The SHAKE (76) algorithm was used to restrain the hydrogen bonds. The cutoff for non-bonded interactions was set to 10 Å. Frames were saved every 25,000 steps, giving a frame rate of 100 ps between each frame. Simulations were performed using the Blue Waters supercomputer(NVIDIA Tesla K20X GPUs) or our in-house computing cluster (NVIDIA GeForce GTX 980 GPUs). Apo-SMO, SAG-SMO, and SANT1-SMO were simulated for a total of ∼250, ∼36, and ∼42 μs, respectively.

Adaptive sampling, feature selection, and clustering

Simulating biological systems using traditional long-MD simulations to observe sub-millisecond dynamics is unfeasible, so we resorted to using a parallel approach to accelerate conformational sampling, called adaptive sampling. The simulation data after every round of simulations were clustered (feature selection explained below), and the least populated clusters were used to seed simulations for the next round. Overall, for Apo-SMO, seven rounds of simulations were performed, collecting 30–50 μs per round. For SAG/SANT1-SMO, the data were collected in a similar fashion, for three rounds each, around 10–20 μs per round. The bias introduced in the system due to selectively starting simulations from least-populated clusters was eliminated by constructing an MSM that estimated the reverse transition probabilities from each microstate.

The progress of the transition from inactive to active was monitored by calculating features, each of which was selected based on maximum magnitude of Δ residue contact score (RRCS). RRCS is an order-parameter-identifying technique that uses a flat-linear-flat scoring scheme to assign a score to contact between every residue pair in the system (6). Contacts that had $|\Delta RRCS| < 3.5$ (58 such distances total) (Table S5) were used. K-means clustering was used to cluster the simulation data, based on these calculated features. Clustering was performed using the pyEMMA python library (85).

MSM construction

The high dimensionality of the data was first reduced using tICA. The tICA lag time was optimized by observing the plateauing of the implied timescales ($-2/\ln\lambda$, λ being the largest eigenvalue of the first tICA eigenvector) vs. the lag time, and was set to 30 ns for the three systems (Apo-SMO, SAG-SMO, SANT1-SMO). The tICA reduced-dimension data were then clustered using k-means clustering. The optimum number of clusters and no. of tICA components to be used was optimized by maximizing the VAMP2 score (sum of the squares of the highest eigenvalues of the transition matrix) for a particular the number of clusters, and the convergence of the implied timescales vs. the MSM lag time. (Figs. S2–S4). Accordingly, the number of clusters was set to 200 (Apo-SMO) and 100 (SANT1-SMO and SAG-SMO). The MSM lag time was set to 30 ns for the three systems (Apo-SMO, SAG-SMO, SANT1-SMO). The Chapman-Kolmogorov test, which tests the validity of the MSM on five macrostates, was performed using pyEMMA (Figs. S5–S7).

Trajectory analysis and visualization

cpptraj (86) was used for trajectory processing. VMD (87,88) and open-source PyMOL (89) were used to visualize and render images. MDTraj (90) was used for computing all order parameters. All plots were made using matplotlib (91) and seaborn (92) python libraries. Numpy (93) was used for numerical computations. The salt-bridge-based contacts were discovered by extracting probability-weighted 10,000 frames from clusters in the inactive, I^{1-3} and active states, using cluster probabilities from the MSM. They were analyzed for unique contacts using GetContacts (94). Tunnel radii for analysis of effect of SAG and SANT1 were calculated using HOLE (95).

Mutual-information calculations

Mutual information for describing the allosteric pathways was computed using mdentropy (96), using the DihedralMutualInformation function. Analysis was performed on 10,000 frames each extracted from Apo-SMO, SANT1-SMO, and SAG-SMO data. The frames were chosen based on the predicted MSM probabilities, to represent the entire ensemble. A graph was constructed from the computed mutual information, and residues with C-α distances <10 Å were considered to be connected by an edge. The weight of each edge was assigned as $MI = MI_{max} - MI_{ab}$, with the MI_{max} as the maximum mutual information computed among two residues in a protein, and MI_{ab} was the mutual information computed between residue pair ab. Edges with $MI < MI_{avg}$ were not considered. This methodology thus adapted has been discussed previously (97–99). The caveats and limitations presented by the methodology—the presence of global dynamics independent of the local dynamics being explored by the limited simulation data (100)—have been resolved by using long-timescale simulations. Allosteric pathways were computed by calculating the shortest paths between two nodes (in our case E518 and W339) using Dijkstra's algorithm (101). NetworkX (102), a python library, was used for graph construction, visualization, and computing shortest paths.

RESULTS AND DISCUSSION

SMO activation involves a conserved molecular switch

To probe the transitions SMO undergoes during activation, SMO was simulated in a ligand-free form (Apo-SMO) from two starting points: inactive and active structures. Simulations were performed using a parallel approach: by clustering the existing data based on selected features (feature selection explained in section "methods") and seeding the next round of simulations by randomly selecting starting points from the least populated clusters, a technique known as adaptive sampling (103) (Fig. S8; Tables S1 and S2). The high dimensionality of the data was reduced by transforming it using time-independent component analysis (tICA) (104,105). tICA uses a linear combination of the supplied features to identify the slowest collective degrees of freedom in the data by computing the time-lagged autocorrelation. The first two tICA components account for the two slowest processes associated with activation (Figs. S9 and S10). The active and inactive structures were separated majorly in the first tICA component (tIC 1), indicating that activation was the slowest process observed in simulations. Hence, features that were highly correlated with tIC 1 (Fig. S11) were considered pivotal to activation. The convergence of the data, clusters, and hence the free energies derived from it were confirmed by the presence of a continuous density of data along tIC 1 (Fig. S9 *A*). This shows that the simulations have indeed sampled the conformational landscape necessary to probe the activation pathway of SMO. The tICA transformed data were clustered, dividing the data into kinetically distinct microstates. An MSM was constructed on the clustered data to compute the transition rates between microstates and to reweigh the data, eliminating the bias introduced by adaptive sampling.

At the intracellular end, we observe that $W339^{3.50f}$ shows a very dramatic reorientation on receptor activation, moving outward from the center of the TM bundle to accommodate the bound G_i. $W339^{3.50f}$ is conserved across all class F receptors (Fig. S12). Upon further analysis, we observed that this rearrangement extends to include $M449^{6.30f}$ and $G453^{6.34f}$ (outward movement), $G422^{5.65f}$ (translation) (Fig. 2 *A*), as well as $W535^{7.55f}$ (inward rotation), residues that are all conserved across the entire class F family (Fig. S12).

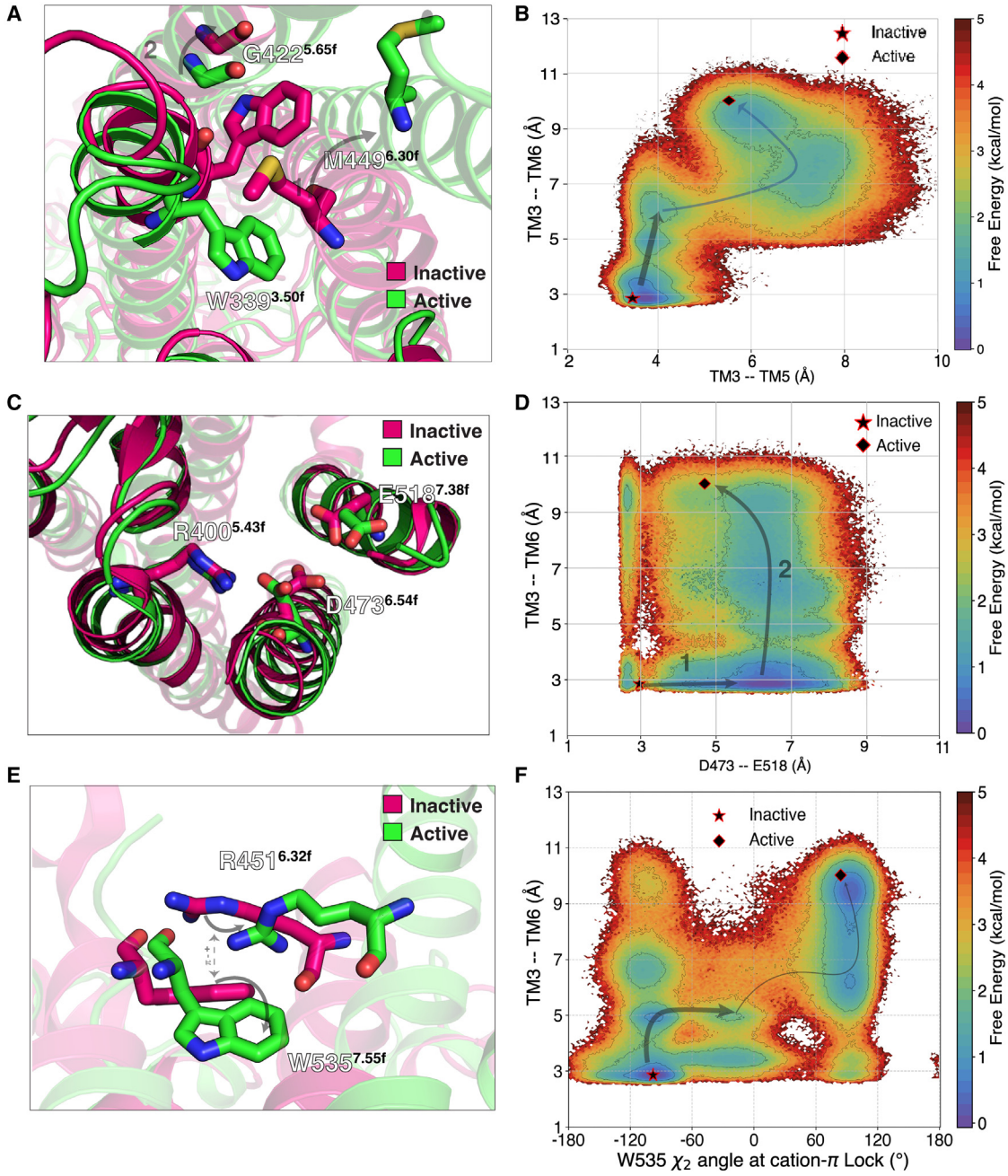

FIGURE 2 Molecular metrics integral to SMO activation. (*A*) Rearrangement of the WGM motif, a conserved molecular switch across class F GPCRs, undergoes rearrangement on SMO activation. (*B*) Relative free energies from MSM-weighted simulation data plotted on the TM3-TM6 distance vs. TM3-TM5 distance measured at residues $W339^{3.50f}$, $M449^{6.30f}$, and $G422^{5.65f}$. (*C*) Breaking of the D-R-E network on the extracellular end of the TMD. (*D*) Similar to (*B*), but for TM3-TM6 distance vs. the D-E distance. (*E*) The π-cation lock breaks by the sidechain rotation of $W535^{7.55f}$. (*F*) Same as (*B*) but for TM3-TM6 distance vs. χ_2 dihedral measured at $W535^{7.55f}$. To see this figure in color, go online.

$M449^{6.30f}$'s outward movement is a proxy for the outward movement of TM6, a process associated with canonical GPCR activation (37,39). However, instead of kinking outward as observed in class B receptors, TM6 in SMO undergoes translation, to accommodate G_i. This can be attributed to the absence of $P^{6.43f}$, a residue conserved across FZDs (Fig. S12). $P^{6.43f}$ is replaced by $F462^{6.43f}$ in SMO, thereby increasing its rigidity and resistance to developing kinks (106). The recently published structure of active FZD7 (107) shows this kink at $P^{6.43f}$. Similar translation in TM6 is observed in rhodopsin, a class A receptor (108). This particular feature is hence unique to the activation mechanism of SMO. TM5, on the other hand, shows slight inward translation. To capture these outlined movements, we projected the entire Apo-SMO data onto $W339^{3.50f}$–$M449^{6.30f}$ (TM3–TM6 distance) vs. $W339^{3.50f}$–$G422^{5.65f}$ (TM3–TM5 distance) and

computed the free energy associated with each state (Figs. 2 *B* and S13). The free-energy plot shows that this TM3-5-6 rearrangement follows a stage-wise process, with TM6 moving outward first by $\sim$ 4 Å (state 1 in Fig. 2 *B*) followed by the rest of the TM3 outward movement after a slight outward rearrangement in TM5 (state 2 in Fig. 2 *B*). The overall free-energy barrier for this rearrangement is $\sim$2.5 kcal/mol. The outward movement of TM6 is analogous to class A receptor activation (Fig. S14 *A* and *B*). A conserved molecular switch mediating SMO's activation on the intracellular end is similar to the breakage of molecular switch E/DRY in class A GPCRs, with W339$^{3.50f}$ being the residue analogous to R$^{3.50}$ (Fig. S14 *C* and *D*). Hence, we posit that this conserved molecular motif (WGM) is integral to class F receptor activation and provides a basis for activation across the entire class F receptors, and also showing the uniqueness of activation of class F receptors.

The crystal structure of SMO bound to the synthetic agonist SAG1.5 gives clues about the activation-specific residue-level rearrangements that occur on the extracellular end of SMO. D473$^{6.54f}$ has been established as a residue critical to SMO activity, as it forms a part of SMO's core TMD ligand-binding cavity, and is shown to interact with agonists SAG1.5, SAG, oxysterols, and antagonists GDC-0449 and AntaXV (34,37,39,109,110). Specifically, a network of salt bridges formed by the residues D473$^{6.54f}$, E518$^{7.38f}$, and R400$^{5.43f}$ is broken in SAG1.5-bound SMO (Fig. 2 *C*) (34). Hence, we also projected the Apo-SMO data on the D473$^{6.54f}$–E518$^{7.38f}$ distance vs. intracellular TM3–6 movement (Figs. 2 *D* and S13). We observe that the TM6–TM3 outward movement (2 in Fig. 2 *D*) is preceded by the breakage of the hydrogen bond between D473$^{6.54f}$ and E518$^{7.38f}$ (1 in Fig. 2 *D*).

To outline the role of the π-cation lock W535$^{7.55f}$–R451$^{6.32f}$ in activation, we projected this π-cation lock contact vs. the TM3–6 outward movement (Figs. 2 *E* and *F* and S13) for Apo-SMO. Projecting the Apo-SMO data along the sidechain dihedral angle χ_2 of W535$^{7.55f}$ clearly showed the distinct inactive and active states. This shows that the mechanism of π-cation lock breaking involves the sidechain rotation of W535$^{7.55f}$. Additionally, we observe that the π-cation lock breaks around the same TM3–TM6 distance as the outward movement of TM3. Thus, the WGM motif and the π-cation lock at the intracellular end, and the D-R-E network at extracellular end, are critical residue networks involved in SMO activation. These residues form a network of allosterically coupled residues, proving crucial for signal transduction across the membrane.

Residues at the CRD–TMD interface involve salt-bridge rearrangements in SMO activation

SMO, in addition to a heptahelical TM domain, possesses an extracellular domain called the CRD. The CRD consists of residues that are highly polar compared with the TMD, which is mostly hydrophobic (Fig. S15). This domain is critical for SMO activation, as SMO Δ CRD mutants show a higher constitutive activity, suggesting that the CRD represses SMO's basal activity (111). The CRD also includes the primary sterol binding site in SMO (32), and it has been posited that PTCH inhibits SMO by reducing cholesterol access to this site (18). Structures of active *Xenopus laevis* SMO (xSMO) show a dramatic reorientation of the CRD on xSMO activation, suggesting that the CRD has a very dynamic range of motion (110). However, this reorientation is not observed in human SMO (hSMO) (32,36). Thus to establish a role of the CRD in activation of hSMO, we sought residue pairs in Apo-SMO CRD–TMD interface that showed the highest variance along tIC1, the slowest process that captured Apo-SMO activation.

Fig. 3 *A*–*F* show the residue pairs that have the highest change in contact frequency during activation, starting with the R485$^{6.66f}$–D209^{CRD} salt-bridge, which breaks during activation (Fig. 3 *A*) due to the outward movement of TM6. This indicates that the R485$^{6.66f}$–D209^{CRD} salt bridge is involved in stabilizing the inward conformation of TM6 in the inactive state. This loss of the R485$^{6.66f}$–D209^{CRD} salt bridge is, however, compensated by the formation of the nearby R161^{CRD}–D486$^{6.67f}$ salt bridge, which is predominantly seen in the active conformation (Fig. 3 *D*). Furthermore, the inactive state shows a salt bridge E208^{CRD}–K395^{ECL2}, which breaks on activation, compensated by the formation of the nearby D201^{CRD}–R296^{ECL1} (Fig. 3 *B* and *E*). Additionally, activation strongly favors the formation of R159^{CRD}–D209^{CRD} (Fig. 3 *C*) and D382^{ECL2}–K204^{CRD} (Fig. 3 *F*) salt bridges. The inactive (green) and active (magenta) structures depicted in the figure were taken as representative structures from the inactive-like and active-like free-energy wells in the tIC landscape.

The path along tIC1 from the inactive state to active state involves three intermediate states (I_{1-3}) (Fig. 4 *A*), characterized by free-energy barriers of at least 1 kcal mol^{-1} among them. Using transition path theory on the constructed MSM, we calculated the fluxes of transitions between these states to establish timescales for activation of SMO (Fig. 4 *B*). The simulations show that the entire process of activation from inactive to active has a mean first passage time (MFPT) of $\sim$72 μs (Fig. 4 *B*), whereas the reverse process is $\sim$3X faster, with MFPT $\sim$ 24 μs.

We observe that residue pair rearrangements that are associated with activation at the CRD–TMD junctions are salt bridges, mostly between residues with one residue in CRD and the other one in TMD (Fig. S16). Almost none of these polar residues are conserved (Figs. S12 and S17), indicating that these residues contribute to a unique activation process for SMO at the CRD–TMD interface. Additionally, we observe that the entire CRD motion can be accounted for by a slight outward rotational motion of the CRD (Fig. S18), thereby causing TM6 to move outward and triggering activation on the intracellular end. Since the CRD has a cholesterol binding site, it is possible that

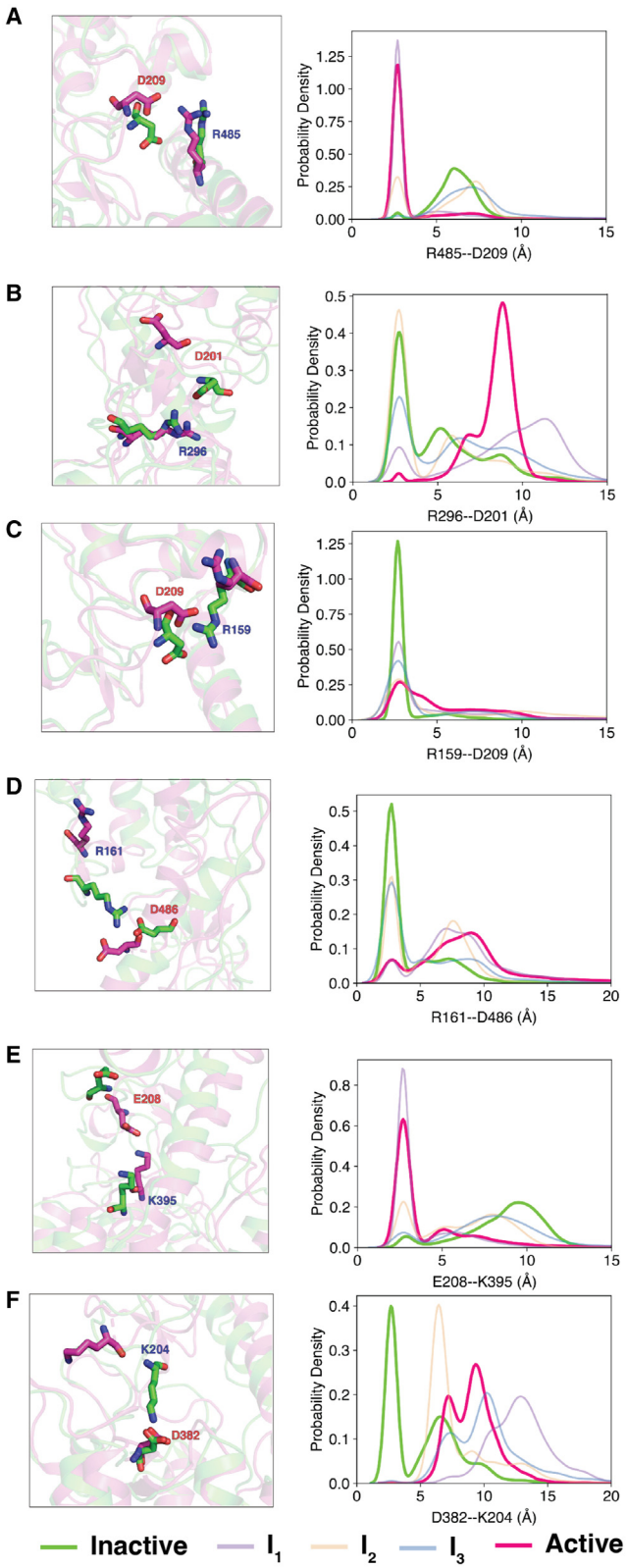

FIGURE 3 Overall activation of SMO involves residues at CRD–TMD junction. Snapshots and probability density plots outlining the salt-bridge rearrangements for (*A*) R485-D209, (*B*) R296-D201, (*C*) R159-D209, (*D*) R161-D486, (*E*) E208-K395, and (*F*) D382-K204 at the CRD–TMD interface during SMO activation. To see this figure in color, go online.

cholesterol binding to the CRD triggers this outward rotation, inducing the signal that causes TM6 to move out. This potentially outlines a mechanism for the activation of SMO by cholesterol, its endogenous agonist.

SMO's activation is linked to opening of a hydrophobic tunnel

Endogenously, on PTCH's inhibition by Shh, SMO is activated. SMO's activation is mediated endogenously by cholesterol, suggesting that PTCH's inhibition facilitates SMO's activation by cholesterol. This suggests that cholesterol from the membrane travels to the extracellular sterol binding site. How this transfer of cholesterol occurs to the SMO CRD is still unknown. However, SMO does indeed present itself with a unique topology, the presence of a tunnel inside the protein. This tunnel has been hypothesized (37–39,110) to facilitate the transport of cholesterol from the membrane to the binding site in the CRD (32), making this tunnel a prime target for inhibitors. As noted by Qi et al., SMO antagonists (SANT1, AntaXV, LY2940680) bind deeper into a tunnel inside SMO, whereas SMO agonists (SAG) bind outside this tunnel. Adding a 4-aminomethyl moiety to the tail end of SAG converts it to an antagonist, suggesting that this added moiety can hinder the tunnel (112). Mutations that introduced a bulky residue into the tunnel (V329F, V333F, V408F, I412F, T470Q), blocked SMO activity (32,38), suggesting that the tunnel conformation was linked to how small molecules and mutations modulated SMO activity (37). This suggests that SMO antagonists such as SANT1 act as steric antagonists by blocking the sterol tunnel inside SMO, whereas agonists such as SAG allosterically activate SMO by breaking the D-R-E network, setting off receptor activation on the intracellular end. The mechanism and dynamics of the modulators acting on SMO's activation is still unclear. Hence we simulated SMO bound to antagonist SANT1 (SANT1-SMO) and agonist SAG (SAG-SMO) to probe the effect of bound agonist and antagonist on SMO's activation.

SMO's tunnel is characterized by markedly hydrophobic residues (Fig. S19), pointing further toward the idea that a hydrophobic molecule may be transported through it. This tunnel runs through the core of the receptor, spans the entire TM domain, starting at the conserved residues $W339^{3.50f}$, spans $\sim$ seven helical turns, and ends at the extracellular network of residues $E518^{7.38f}$, $D473^{6.54f}$, and $R400^{5.43f}$. These three residues form the base of the space between the CRD and TMD. Moving outward along the path defined along the tunnel directly leads to the binding site, with TM6, ECL2, and ECL1 forming the bridge between these sites (Fig. S20).

In SANT1-SMO simulations, the tunnel remains almost completely blocked (Fig. 5 *A* and *B*), indicating that the mechanism by which SANT1 modulates SMO activity is by binding deeply into the SMO tunnel core, precluding

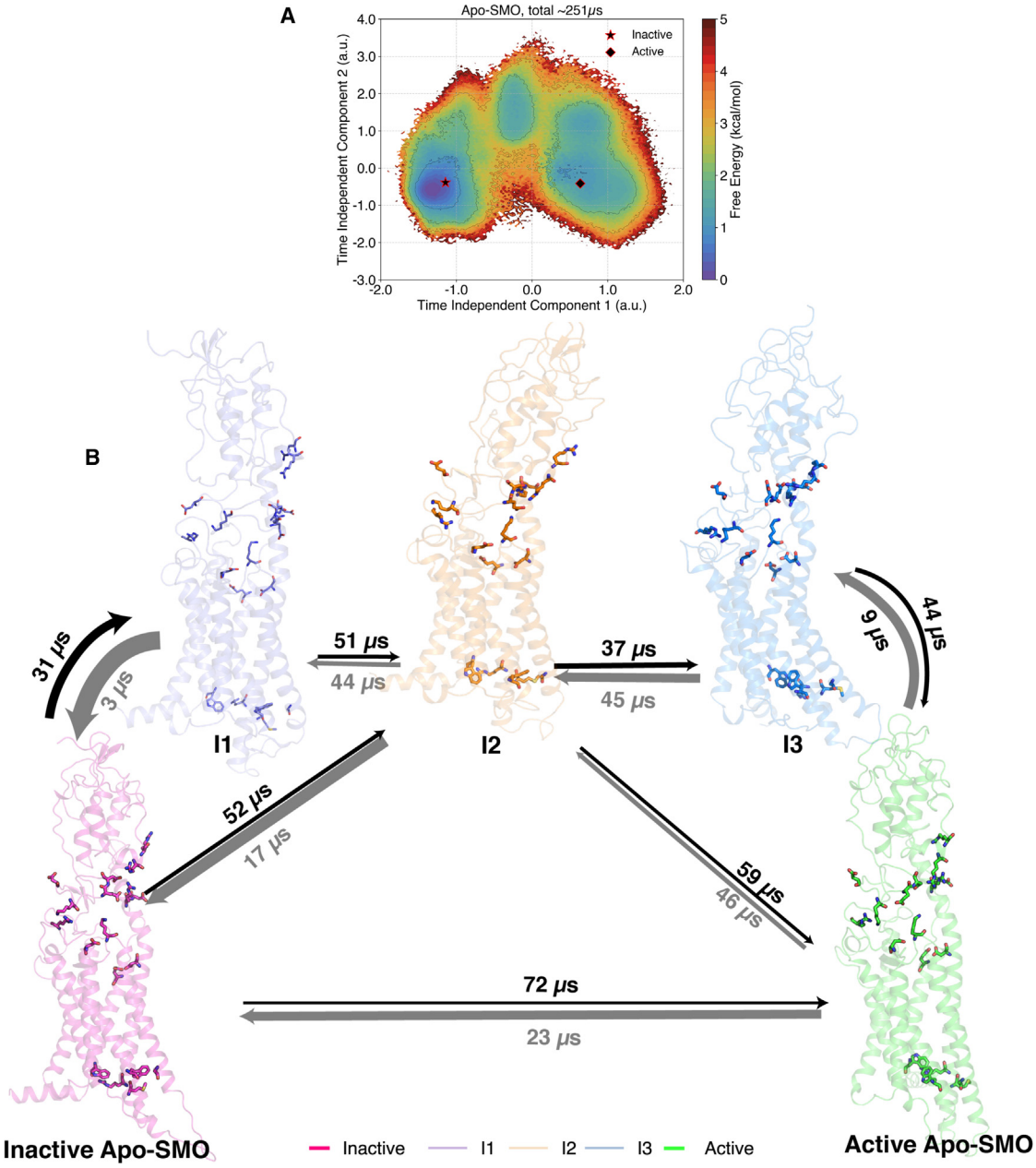

FIGURE 4 (*A*) Relative free energies from MSM-weighted simulation data of Apo-SMO plotted along tIC1 and tIC2, the two slowest components, with the intermediate states I_{1-3} as shown. The intermediate states I_{1-3} were defined based on metastable basins and free-energy barriers associated with transitioning from an inactive to an active state. A cutoff of 1.8 kcal/mol was used to separate one basin from another. Residues shown as sticks include the π-cation lock, the WGM motif, and the salt bridges involved in activation. (*B*) Overall transition pathway of SMO activation process. The inactive (PDB: 5L7D) (32) and active (PDB: 6XBL) (37) structures are separated by the presence of three metastable conformations in between, I_{1-3}. Residues shown by sticks correspond to the salt bridges, the WGM motif, the D-R-E network, and the π-cation lock, all residues critical for mediating SMO activation. To see this figure in color, go online.

the potential transport of cholesterol. SANT1's piperazine moiety directly interacts with $H470^{6.51f}$ and sidechain of $M525^{7.45f}$, forming hydrogen bond interactions. The pyrrolic head of the ligand remains buried deep inside, with minimal movement normal to the plane of the membrane, along the tunnel (Fig. S21). However, in Apo-SMO simulations, the tunnel remains relatively open (Fig. 5 *C* and *D*). Interestingly, we observe a conformational dependence of the lipid organization in the membrane; inactive SMO surrounds itself with a cholesterol in the upper leaflet, as opposed to other cases (Fig. S22). This suggests that cholesterol shows a propensity to accumulate outside inactive SMO to possibly transport itself in the hydrophobic tunnel, leading to SMO activation. Additionally, in SAG-SMO simulations, we observe that the tunnel radius has a sudden kink outward ($z \sim -20$ Å), suggesting that there is a relative expansion of

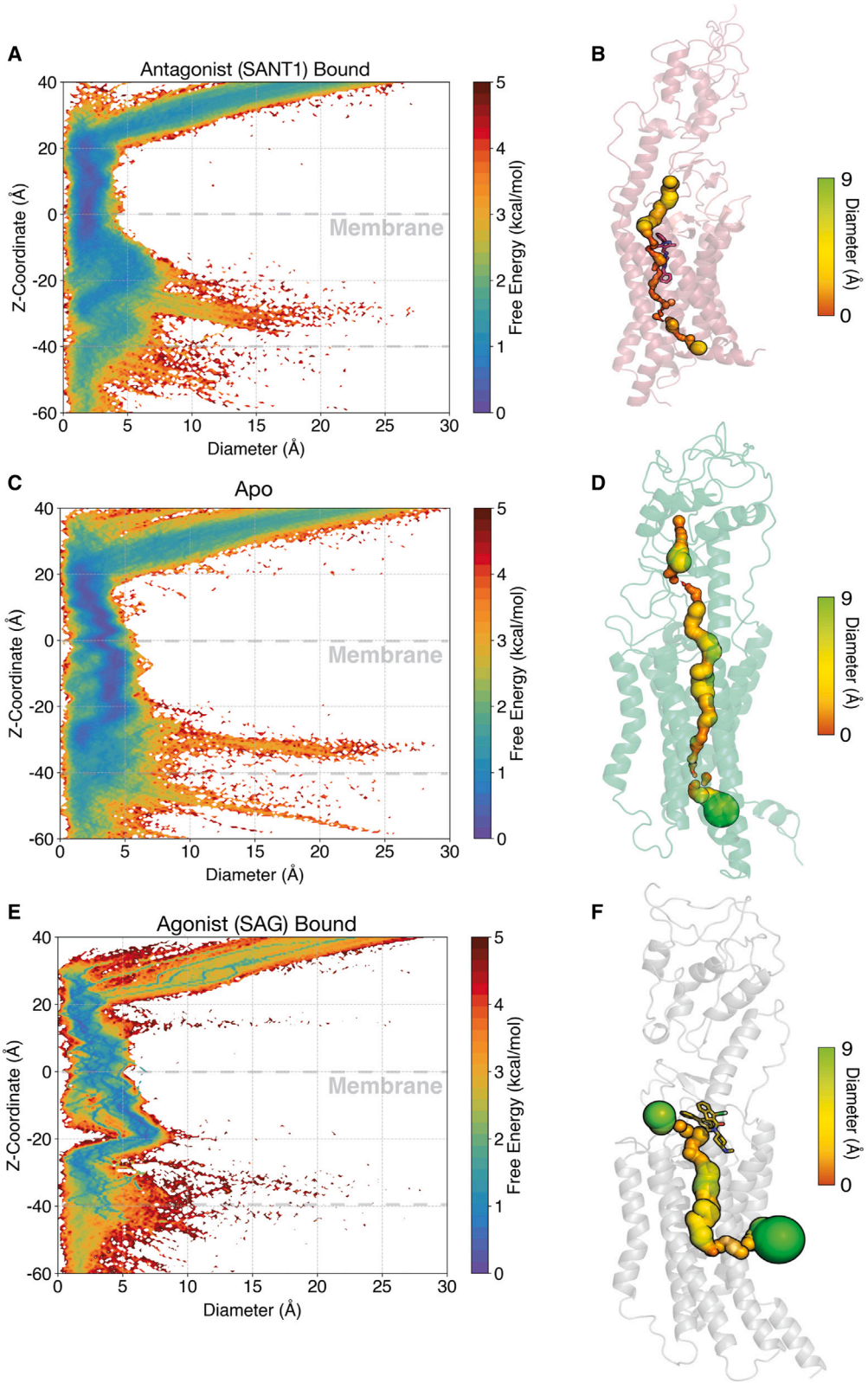

FIGURE 5 Tunnel radius plots for SMO. (*A*) Free-energy plot of the tunnel diameter along the z coordinate for SANT1-bound SMO. (*C*) same as (*A*), but for Apo-SMO. (*E*) Same as (*A*), but for SAG-bound SMO. SAG-bound SMO clearly shows the expansion of the tunnel compared with Apo-SMO and SANT1-SMO. (*B*) SANT-1 SMO, (*D*) Apo-SMO, and (*F*) SAG-SMO shown with a representative tunnel. Tunnel radii were calculated using the HOLE program (95). To see this figure in color, go online.

the tunnel induced by SAG (Fig. 5 *E* and *F*). In the simulations, the membrane extends from z = 0 to z = −40. Since this expansion occurs between z = 0 and z ∼ −20 Å, it suggests the opening is in the upper leaflet (Fig. S24 *A*). On plotting the free-energy difference between Apo-SMO and SAG-SMO, a marked difference in the free energy associated with the opening of the tunnel is observed (Fig. S23 *A*–*C*). Recent studies suggest that active PTCH precludes SMO's accessibility to cholesterol in the upper leaflet (20). To further probe into the exact position of this tunnel opening, we observed that a cluster of openings occurred at x ∼ 16 Å and y ∼ 22 Å, corresponding to the space between TM2 and TM3 (Fig. S24 *B*). This is in agreement with a recent study that used coarse-grained simulations to observe a cholesterol binding site at the TM2–TM3 interface in the upper leaflet (113). Thus, SAG acts as an agonist by allosterically expanding the tunnel at the cholesterol interaction site, giving further evidence for the cholesterol-transport-like activity of SMO. Thus we conclude that SANT1 functions as a steric antagonist by blocking the tunnel, whereas SAG functions by allosterically expanding the tunnel, thereby establishing design rules for SMO agonists and antagonists.

SAG alters the allosteric pathways in SMO during the process of SMO activation

To further investigate the mechanism by which SAG allosterically modulates SMO's activity resulting in the expansion of the tunnel, we computed the allosteric pathways that connected the intra- and extracellular ends of SMO, responsible for transmembrane signal transduction. Allosteric pathways contain a series of conformationally coupled residues that link dynamically active and spatially distant residues. In class A GPCRs, allosteric pathways are responsible for communicating conformational changes from the extracellular end to the intracellular end, completing the process of signal transduction (97–99). Since SMO's activation process involves allosteric communication between the extracellular ligand binding site (D-R-E network) and the G protein-coupling site (WGM motif), we sought to analyze the allosteric pathways that connect the two sites. We computed the dynamic pairwise mutual information of inactive-Apo-SMO, active-Apo-SMO, SANT1-SMO, and SAG-SMO on a residue-level basis, and constructed a graphical network of residues that are allosterically linked. The dynamic mutual information takes into account the residue-level movements. Based on this network, we present the allosteric pathway between the intra- and extracellular ends of TMD.

In our simulations, we observe that the allosteric pathway between the intra- and extracellular ends in Apo-inactive SMO completely passes through TM6, encompassing residues T466$^{6.47f}$, F460$^{6.41f}$, and G456$^{6.37f}$ (Fig. 6 *A*). This establishes an integral role for TM6 in mediating the signals across the transmembrane domain in inactive SMO. SANT1-SMO on the other hand, unexpectedly shows a distinct pathway, first going down intra-helically to A524$^{7.24f}$, crossing over to TM6 via A459$^{6.40f}$, and finally to L335$^{3.46f}$ (Fig. 6 *B*). This, however, can be explained by the observation that the SANT1 causes a slight outward movement of TM6, to accommodate itself in the deep core TMD ligand binding cavity (Fig. S25). This outward movement of TM6 moves T466$^{4.67f}$ away from E518$^{7.55f}$. This causes the network to rearrange itself, moving over to TM6 further downstream. On the other hand, SAG and

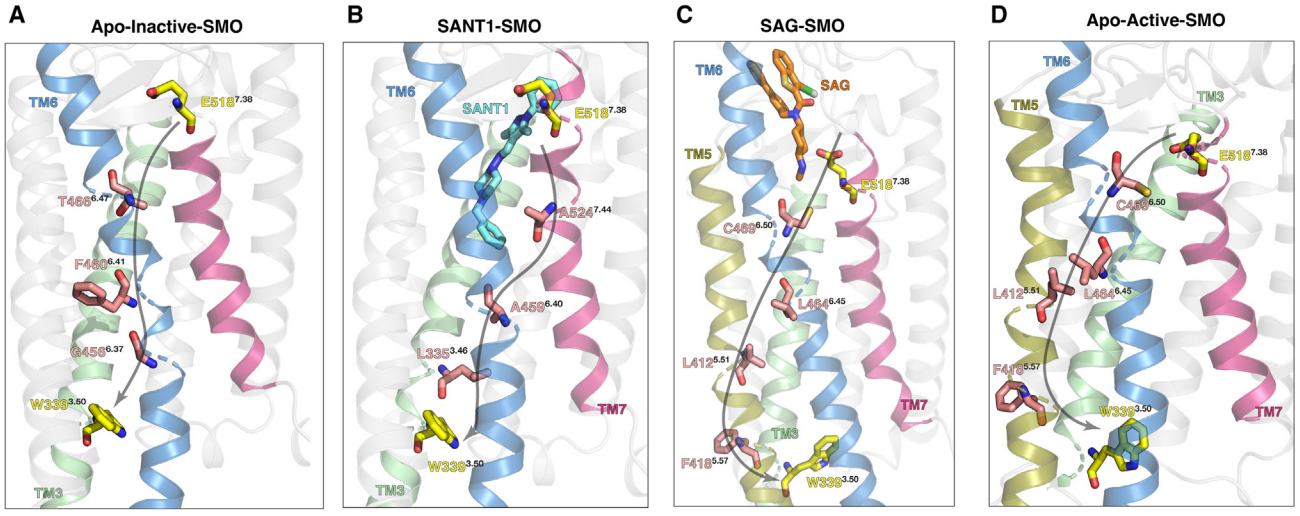

FIGURE 6 Allosteric pathways between E518$^{7.38f}$ and W339$^{3.50f}$. (*A*) Pathway in Apo-inactive SMO. Since the tunnel radius is decreased, TM6 outward movement is restricted, and therefore the entire allosteric communications occurs via TM6. (*B*) In SANT1-SMO, due to slight outward movement of TM6, the pathways switches from TM7 to TM6 to TM3. (*C* and *D*) SAG-SMO and Apo-active SMO show the same allosteric pathway, which spans TM7-TM6-TM5-TM3. To see this figure in color, go online.

Apo-active SMO show the exact same networks, further indicating that SAG alters the allosteric networks in SMO to resemble active SMO. These networks involve C469$^{6.50f}$, the most conserved residue in TM6, down L464$^{6.45f}$, and a flip over to TM5 as we move intracellularly, due to the outward intracellular movement of TM6, via L412$^{5.55f}$ and F418$^{5.61f}$ (Fig. 6 *C* and *D*). Thus, we can establish a basis for the mechanisms through which SAG and SANT1 effectively modulate SMO activity, and establish an integral role for TMs 7, 6, 5, and 3 in signal transduction.

CONCLUSIONS

Our study reveals the activation mechanism for SMO, a class F GPCR, in atomistic detail via molecular dynamics simulations. We characterized the residue-level transitions that SMO undergoes during activation. We simulated SMO in Apo-, SAG-, and SANT1-bound states to probe the activation mechanism of SMO, and computed the free-energy landscape of the process. Our MSM-weighted free-energy landscapes show a barrier of maximal free-energy barrier of ~ 3 kcal mol^{-1} while transitioning from an inactive to active state, involving three intermediate states.

Class A and class B receptors have been the subject of major interest involving GPCR activation (4,9). Receptor activation studies on class F majorly focused on the start and end states of the receptor, without giving an overview of the dynamics of the process. Using computational methods, we show that SMO activation involves the rearrangement of an intracellular structural motif, the WGM motif, conserved across the entire class F family. This lays the basis for a common activation mechanism for all class F receptors on the intracellular end. Additionally, this motif involves W$^{3.50f}$, which is the residue equivalent to R$^{3.50}$ in class A receptors, establishing the integral role of TM3 in GPCR activation. On the extracellular end of TMD, we see that the D-R-E network of residues is pivotal to activation, as it engages the agonist and sets off the activation process at the intracellular end. We also show evidence of allosteric coupling between these two sites, showing that the rearrangement of the D-R-E network is necessary to ensure intracellular rearrangement of the WGM motif.

We also establish a role for the CRD in SMO activation, forming and breaking salt bridges while transitioning to an active state, contacts that have not been discussed previously. This gives novelty to the methodology established, implying that MD simulations can be used to discover contacts crucial to activation, which was previously unknown. We show that the agonist SAG expands an intra-TMD tunnel inside SMO, further supporting the hypothesis that SMO transports a cholesterol molecule through its hydrophobic tunnel to activate SMO (19,20,37,39,110). We also show that SAG acts as an allosteric modulator by modifying SMO's allosteric pathways to be similar to Apo-SMO. On the other hand, SANT1 acts as a steric antagonist, by occluding the hydrophobic tunnel inside SMO, hence lowering the radius. Therefore, we establish the mechanisms of action of antagonists and agonists in modulating SMO activity. Additionally, experimental validation by mutagenesis of the role of various residues needs to be performed for further corroboration of this computational study. Mutation of residues of the WGM motif (W339, G422, M449), the various salt bridges, the interface of upper leaflet and TM2–3, and the allosterically coupled residues, possibly through techniques such as alanine scans and deep mutagenesis, can be performed as testable hypotheses, thereby delineating the role of these residues in modulating SMO activity. Additionally, how cholesterol, the endogenous agonist of SMO, modulates SMO activity in the presence of agonists still needs to be explored. However, we propose that the overall mechanistic findings from this study can be used to design novel SMO antagonists for chemotherapy.

DATA AVAILABILITY

Stripped trajectories and corresponding parameter files have been uploaded to Box (https://uofi.box.com/s/c12lwov1mtrncm30hydu9iqhb45dcwx4). Scripts used for MSM construction and trajectory analysis have been uploaded to GitHub (https://github.com/ShuklaGroup/Bansal_et_al_Smoothened_Activation_2022).

SUPPORTING MATERIAL

Supporting material can be found online at https://doi.org/10.1016/j.bpj.2023.03.007.

AUTHOR CONTRIBUTIONS

D.S. designed the research. P.D.B. performed simulations. P.D.B. and S.D. analyzed the data. P.D.B. wrote the manuscript with inputs from S.D. and D.S.

ACKNOWLEDGMENTS

The authors thank The Blue Waters Petascale Computing Facility and National Center for Supercomputing Applications, which is supported by the National Science Foundation (awards OCI-0725070 and ACI-1238993) and the state of Illinois. Blue Waters is a joint effort of the University of Illinois at Urbana-Champaign and its National Center for Supercomputing Applications. D.S. acknowledges support from NIH grant R35GM142745 and Cancer Center at Illinois. P.D.B thanks Austin Weigle and Jiming Chen of the Shukla Group at University of Illinois for their valuable insights throughout the course of this study.

DECLARATION OF INTERESTS

The authors declare no competing interests.

SUPPORTING CITATIONS

References (114–117) appear in the supporting material.

REFERENCES

1. Riobo, N. A., B. Saucy, …, D. R. Manning. 2006. Activation of heterotrimeric G proteins by smoothened. *Proc. Natl. Acad. Sci. USA.* 103:12607–12612. https://doi.org/10.1073/pnas.0600880103.
2. Ogden, S. K., D. L. Fei, …, D. J. Robbins. 2008. G protein Gαi functions immediately downstream of Smoothened in Hedgehog signalling. *Nature.* 456:967–970. https://doi.org/10.1038/nature07459.
3. Chen, W., X.-R. Ren, …, R. J. Lefkowitz. 2004. Activity-dependent internalization of smoothened mediated by ß-arrestin 2 and GRK2. *Science.* 306:2257–2260. https://doi.org/10.1126/science.1104135.
4. Weis, W. I., and B. K. Kobilka. 2018. The molecular basis of G protein–coupled receptor activation. *Annu. Rev. Biochem.* 87:897–919. https://doi.org/10.1146/annurev-biochem-060614-033910.
5. Latorraca, N. R., A. J. Venkatakrishnan, and R. O. Dror. 2017. GPCR dynamics: structures in motion. *Chem. Rev.* 117:139–155. https://doi.org/10.1021/acs.chemrev.6b00177.
6. Zhou, Q., D. Yang, …, S. Zhao. 2019. Common activation mechanism of class A GPCRs. *Elife.* 8:e50279. https://doi.org/10.7554/elife.50279.
7. Nygaard, R., Y. Zou, …, B. K. Kobilka. 2013. The dynamic process of β2-adrenergic receptor activation. *Cell.* 152:532–542. https://doi.org/10.1016/j.cell.2013.01.008.
8. Kohlhoff, K. J., D. Shukla, …, V. S. Pande. 2014. Cloud-based simulations on Google Exacycle reveal ligand modulation of GPCR activation pathways. *Nat. Chem.* 6:15–21. https://doi.org/10.1038/nchem.1821.
9. Mattedi, G., S. Acosta-Gutiérrez, …, F. L. Gervasio. 2020. A combined activation mechanism for the glucagon receptor. *Proc. Natl. Acad. Sci. USA.* 117:15414–15422. https://doi.org/10.1073/pnas.1921851117.
10. Wang, C., H. Wu, …, R. C. Stevens. 2013. Structure of the human smoothened receptor bound to an antitumour agent. *Nature.* 497:338–343. https://doi.org/10.1038/nature12167.
11. Sriram, K., and P. A. Insel. 2018. G protein-coupled receptors as targets for approved drugs: how many targets and how many drugs? *Mol. Pharmacol.* 93:251–258. https://doi.org/10.1124/mol.117.111062.
12. Logan, C. Y., and R. Nusse. 2004. The WNT signaling pathway in development and disease. *Annu. Rev. Cell Dev. Biol.* 20:781–810. https://doi.org/10.1146/annurev.cellbio.20.010403.113126.
13. Riddle, R. D., R. L. Johnson, …, C. Tabin. 1993. Sonic hedgehog mediates the polarizing activity of the ZPA. *Cell.* 75:1401–1416. https://doi.org/10.1016/0092-8674(93)90626-2.
14. Briscoe, J., and P. P. Thérond. 2013. The mechanisms of Hedgehog signalling and its roles in development and disease. *Nat. Rev. Mol. Cell Biol.* 14:416–429. https://doi.org/10.1038/nrm3598.
15. Lee, R. T. H., Z. Zhao, and P. W. Ingham. 2016. Hedgehog signalling. *Development.* 143:367–372. https://doi.org/10.1242/dev.120154.
16. GTEx tissue expression project. https://www.gtexportal.org/home/gene/SMO.
17. Chen, Y., and G. Struhl. 1996. Dual roles for patched in sequestering and transducing hedgehog. *Cell.* 87:553–563. https://doi.org/10.1016/s0092-8674(00)81374-4.
18. Kong, J. H., C. Siebold, and R. Rohatgi. 2019. Biochemical mechanisms of vertebrate hedgehog signaling. *Development.* 146:dev166892. https://doi.org/10.1242/dev.166892.
19. Kinnebrew, M., E. J. Iverson, …, R. Rohatgi. 2019. Cholesterol accessibility at the ciliary membrane controls hedgehog signaling. *Elife.* 8:e50051. https://doi.org/10.7554/elife.50051.
20. Kinnebrew, M., G. Luchetti, …, R. Rohatgi. 2021. Patched 1 reduces the accessibility of cholesterol in the outer leaflet of membranes. *Elife.* 10:e70504. https://doi.org/10.7554/elife.70504.
21. Nieuwenhuis, E., and C. c. Hui. 2005. Hedgehog signaling and congenital malformations. *Clin. Genet.* 67:193–208. https://doi.org/10.1111/j.1399-0004.2004.00360.x.
22. Keeler, R. F. 1969. Toxic and teratogenic alkaloids of western range plants. *J. Agric. Food Chem.* 17:473–482. https://doi.org/10.1021/jf60163a012.
23. Heretsch, P., L. Tzagkaroulaki, and A. Giannis. 2010. Cyclopamine and hedgehog signaling: chemistry, biology, medical perspectives. *Angew. Chem. Int. Ed. Engl.* 49:3418–3427. https://doi.org/10.1002/anie.200906967.
24. Taipale, J., J. K. Chen, …, P. A. Beachy. 2000. Effects of oncogenic mutations in Smoothened and Patched can be reversed by cyclopamine. *Nature.* 406:1005–1009. https://doi.org/10.1038/35023008.
25. Chen, J. K., J. Taipale, …, P. A. Beachy. 2002. Inhibition of Hedgehog signaling by direct binding of cyclopamine to Smoothened. *Genes Dev.* 16:2743–2748. https://doi.org/10.1101/gad.1025302.
26. Nachtergaele, S., D. M. Whalen, …, R. Rohatgi. 2013. Structure and function of the Smoothened extracellular domain in vertebrate Hedgehog signaling. *Elife.* 2:e01340. https://doi.org/10.7554/elife.01340.
27. Corcoran, R. B., and M. P. Scott. 2006. Oxysterols stimulate Sonic hedgehog signal transduction and proliferation of medulloblastoma cells. *Proc. Natl. Acad. Sci. USA.* 103:8408–8413. https://doi.org/10.1073/pnas.0602852103.
28. Raleigh, D. R., and J. F. Reiter. 2019. Misactivation of Hedgehog signaling causes inherited and sporadic cancers. *J. Clin. Invest.* 129:465–475. https://doi.org/10.1172/jci120850.
29. Axelson, M., K. Liu, …, R. Pazdur. 2013. US Food and Drug Administration approval: vismodegib for recurrent, locally advanced, or metastatic basal cell carcinoma. *Clin. Cancer Res.* 19:2289–2293. https://doi.org/10.1158/1078-0432.CCR-12-1956.
30. Jain, S., R. Song, and J. Xie. 2017. Sonidegib: mechanism of action, pharmacology, and clinical utility for advanced basal cell carcinomas. *OncoTargets Ther.* 10:1645–1653. https://doi.org/10.2147/ott.s130910.
31. Meani, R. E., S.-W. Lim, …, J. W. Kelly. 2014. Emergence of chemoresistance in a metastatic basal cell carcinoma patient after complete response to hedgehog pathway inhibitor vismodegib (GDC-0449). *Australas. J. Dermatol.* 55:218–221. https://doi.org/10.1111/ajd.12196.
32. Byrne, E. F. X., R. Sircar, …, C. Siebold. 2016. Structural basis of Smoothened regulation by its extracellular domains. *Nature.* 535:517–522. https://doi.org/10.1038/nature18934.
33. Huang, P., D. Nedelcu, …, A. Salic. 2016. Cellular cholesterol directly activates smoothened in hedgehog signaling. *Cell.* 166:1176–1187.e14. https://doi.org/10.1016/j.cell.2016.08.003.
34. Wang, C., H. Wu, …, R. C. Stevens. 2014. Structural basis for Smoothened receptor modulation and chemoresistance to anticancer drugs. *Nat. Commun.* 5:4355. https://doi.org/10.1038/ncomms5355.
35. Weierstall, U., D. James, …, V. Cherezov. 2014. Lipidic cubic phase injector facilitates membrane protein serial femtosecond crystallography. *Nat. Commun.* 5:3309. https://doi.org/10.1038/ncomms4309.
36. Zhang, X., F. Zhao, …, F. Xu. 2017. Crystal structure of a multidomain human smoothened receptor in complex with a super stabilizing ligand. *Nat. Commun.* 8:15383. https://doi.org/10.1038/ncomms15383.
37. Qi, X., L. Friedberg, …, X. Li. 2020. Sterols in an intramolecular channel of Smoothened mediate Hedgehog signaling. *Nat. Chem. Biol.* 16:1368–1375. https://doi.org/10.1038/s41589-020-0646-2.
38. Deshpande, I., J. Liang, …, A. Manglik. 2019. Smoothened stimulation by membrane sterols drives Hedgehog pathway activity. *Nature.* 571:284–288. https://doi.org/10.1038/s41586-019-1355-4.
39. Qi, X., H. Liu, …, X. Li. 2019. Cryo-EM structure of oxysterol-bound human Smoothened coupled to a heterotrimeric Gi. *Nature.* 571:279–283. https://doi.org/10.1038/s41586-019-1286-0.
40. Wright, S. C., P. Kozielewicz, …, G. Schulte. 2019. A conserved molecular switch in Class F receptors regulates receptor activation and pathway selection. *Nat. Commun.* 10:667. https://doi.org/10.1038/s41467-019-08630-2.
41. Ballesteros, J. A., and H. Weinstein. 1995. [19] Integrated methods for the construction of three-dimensional models and computational probing of structure-function relations in G protein-coupled receptors.

Methods Neurosci. 25:366–428. https://doi.org/10.1016/s1043-9471(05)80049-7.

42. Radhakrishnan, A., R. Rohatgi, and C. Siebold. 2020. Cholesterol access in cellular membranes controls Hedgehog signaling. *Nat. Chem. Biol.* 16:1303–1313. https://doi.org/10.1038/s41589-020-00678-2.
43. Husic, B. E., and V. S. Pande. 2018. Markov state models: from an art to a science. *J. Am. Chem. Soc.* 140:2386–2396. https://doi.org/10.1021/jacs.7b12191.
44. Shukla, D., C. X. Hernández, …, V. S. Pande. 2015. Markov state models provide insights into dynamic modulation of protein function. *Acc. Chem. Res.* 48:414–422. https://doi.org/10.1021/ar5002999.
45. Chan, M. C., B. Selvam, …, D. Shukla. 2022. The substrate import mechanism of the human serotonin transporter. *Biophys. J.* 121:715–730. https://doi.org/10.1016/j.bpj.2022.01.024.
46. Selvam, B., Y.-C. Yu, …, D. Shukla. 2019. Molecular basis of the glucose transport mechanism in plants. *ACS Cent. Sci.* 5:1085–1096. https://doi.org/10.1021/acscentsci.9b00252.
47. Selvam, B., S. Mittal, and D. Shukla. 2018. Free energy landscape of the complete transport cycle in a key bacterial transporter. *ACS Cent. Sci.* 4:1146–1154. https://doi.org/10.1021/acscentsci.8b00330.
48. Ferruz, N., S. Doerr, …, G. De Fabritiis. 2018. Dopamine D3 receptor antagonist reveals a cryptic pocket in aminergic GPCRs. *Sci. Rep.* 8:897. https://doi.org/10.1038/s41598-018-19345-7.
49. Taylor, B. C., C. T. Lee, and R. E. Amaro. 2019. Structural basis for ligand modulation of the CCR2 conformational landscape. *Proc. Natl. Acad. Sci. USA.* 116:8131–8136. https://doi.org/10.1073/pnas.1814131116.
50. Dutta, S., B. Selvam, and D. Shukla. 2022. Distinct binding mechanisms for allosteric sodium ion in cannabinoid receptors. *ACS Chem. Neurosci.* 13:379–389. https://doi.org/10.1021/acschemneuro.1c00760.
51. Dutta, S., B. Selvam, …, D. Shukla. 2022. Mechanistic origin of partial agonism of tetrahydrocannabinol for cannabinoid receptors. *J. Biol. Chem.* 298:101764. https://doi.org/10.1016/j.jbc.2022.101764.
52. Chen, Y., O. Fleetwood, …, L. Delemotte. 2021. Allosteric effect of nanobody binding on ligand-specific active states of the β2 adrenergic receptor. *J. Chem. Inf. Model.* 61:6024–6037. https://doi.org/10.1021/acs.jcim.1c00826.
53. Selvam, B., Z. Shamsi, and D. Shukla. 2018. Universality of the sodium ion binding mechanism in class A G-protein-coupled receptors. *Angew. Chem. Int. Ed. Engl.* 57:3048–3053. https://doi.org/10.1002/anie.201708889.
54. Kapoor, A., G. Martinez-Rosell, …, M. Filizola. 2017. Dynamic and kinetic elements of μ-opioid receptor functional selectivity. *Sci. Rep.* 7:11255. https://doi.org/10.1038/s41598-017-11483-8.
55. Kapoor, A., D. Provasi, and M. Filizola. 2020. Atomic-level characterization of the methadone-stabilized active conformation of μ-opioid receptor. *Mol. Pharmacol.* 98:475–486. https://doi.org/10.1124/mol.119.119339.
56. Shukla, D., M. Lawrenz, and V. S. Pande. 2015. Elucidating ligand-modulated conformational landscape of gpcrs using cloud-computing approaches. *Methods Enzymol.* 557:551–572. https://doi.org/10.1016/bs.mie.2014.12.007.
57. Eswar, N., B. Webb, …, A. Sali. 2006. Comparative protein structure modeling using modeller. *Curr. Protoc. Bioinformatics.* 15:Uni5.6. https://doi.org/10.1002/0471250953.bi0506s15.
58. Gordon, J. C., J. B. Myers, …, A. Onufriev. 2005. H++: a server for estimating pKas and adding missing hydrogens to macromolecules. *Nucleic Acids Res.* 33:W368–W371. https://doi.org/10.1093/nar/gki464.
59. Jo, S., T. Kim, …, W. Im. 2008. CHARMM-GUI: a web-based graphical user interface for CHARMM. *J. Comput. Chem.* 29:1859–1865. https://doi.org/10.1002/jcc.20945.
60. Lee, J., D. S. Patel, …, W. Im. 2019. CHARMM-GUI membrane builder for complex biological membrane simulations with glycolipids and lipoglycans. *J. Chem. Theory Comput.* 15:775–786. https://doi.org/10.1021/acs.jctc.8b01066.
61. Klauda, J. B., R. M. Venable, …, R. W. Pastor. 2010. Update of the CHARMM all-atom additive force field for lipids: validation on six lipid types. *J. Phys. Chem. B.* 114:7830–7843. https://doi.org/10.1021/jp101759q.
62. Best, R. B., X. Zhu, …, A. D. MacKerell. 2012. Optimization of the additive CHARMM all-atom protein force field targeting improved sampling of the backbone φ, ψ and side-chain χ1 and χ2 dihedral angles. *J. Chem. Theory Comput.* 8:3257–3273. https://doi.org/10.1021/ct300400x.
63. Marino, K. A., and M. Filizola. 2017. Investigating small-molecule ligand binding to G protein-coupled receptors with biased or unbiased molecular dynamics simulations. *Methods Mol. Biol.* 1705:351–364. https://doi.org/10.1007/978-1-4939-7465-8_17.
64. Ribeiro, J. M. L., and M. Filizola. 2019. Insights from molecular dynamics simulations of a number of G-protein coupled receptor targets for the treatment of pain and opioid use disorders. *Front. Mol. Neurosci.* 12:207. https://doi.org/10.3389/fnmol.2019.00207.
65. Lu, S., X. He, Z. Yang, …, J. Zhang. 2021. Activation pathway of a G protein-coupled receptor uncovers conformational intermediates as targets for allosteric drug design. *Nat. Commun.* 12:4721. https://doi.org/10.1038/s41467-021-25020-9.
66. Hedderich, J. B., M. Persechino, …, P. Kolb. 2022. The pocketome of G-protein-coupled receptors reveals previously untargeted allosteric sites. *Nat. Commun.* 13:2567. https://doi.org/10.1038/s41467-022-29609-6.
67. CGenFF interface at paramchem. https://cgenff.umaryland.edu/.
68. Vanommeslaeghe, K., E. Hatcher, …, A. D. Mackerell. 2010. CHARMM general force field: a force field for drug-like molecules compatible with the CHARMM all-atom additive biological force fields. *J. Comput. Chem.* 31:671–690. https://doi.org/10.1002/jcc.21367.
69. Vanommeslaeghe, K., E. P. Raman, and A. D. MacKerell. 2012. Automation of the CHARMM general force field (CGenFF) II: assignment of bonded parameters and partial atomic charges. *J. Chem. Inf. Model.* 52:3155–3168. https://doi.org/10.1021/ci3003649.
70. Turney, J. M., A. C. Simmonett, …, T. D. Crawford. 2011. Psi4: an open-source *ab-initio* electronic structure program. *WIREs. Comput. Mol. Sci.* 2:556–565. https://doi.org/10.1002/wcms.93.
71. Lee, J., X. Cheng, …, W. Im. 2016. CHARMM-GUI input generator for NAMD, GROMACS, AMBER, OpenMM, and CHARMM/OpenMM simulations using the CHARMM36 additive force field. *J. Chem. Theory Comput.* 12:405–413. https://doi.org/10.1021/acs.jctc.5b00935.
72. Scandroglio, F., J. K. Venkata, …, S. Sonnino. 2008. Lipid content of brain, brain membrane lipid domains, and neurons from acid sphingomyelinase deficient mice. *J. Neurochem.* 107:329–338. https://doi.org/10.1111/j.1471-4159.2008.05591.x.
73. Jorgensen, W. L., J. Chandrasekhar, …, M. L. Klein. 1983. Comparison of simple potential functions for simulating liquid water. *J. Chem. Phys.* 79:926–935. https://doi.org/10.1063/1.445869.
74. Hopkins, C. W., S. Le Grand, …, A. E. Roitberg. 2015. Long-time-step molecular dynamics through hydrogen mass repartitioning. *J. Chem. Theory Comput.* 11:1864–1874. https://doi.org/10.1021/ct5010406.
75. Case, D., K. Belfon, …, and R. Duke. AMBER 2018. University of California .
76. Andersen, H. C. 1983. Rattle: a "velocity" version of the shake algorithm for molecular dynamics calculations. *J. Comput. Phys.* 52:24–34. https://doi.org/10.1016/0021-9991(83)90014-1.
77. Salomon-Ferrer, R., D. A. Case, and R. C. Walker. 2012. An overview of the Amber biomolecular simulation package. *WIREs. Comput. Mol. Sci.* 3:198–210. https://doi.org/10.1002/wcms.1121.
78. Case, D. A., T. E. Cheatham, …, R. J. Woods. 2005. The Amber biomolecular simulation programs. *J. Comput. Chem.* 26:1668–1688. https://doi.org/10.1002/jcc.20290.

79. Götz, A. W., M. J. Williamson, …, R. C. Walker. 2012. Routine microsecond molecular dynamics simulations with AMBER on GPUs. 1. Generalized born. *J. Chem. Theory Comput.* 8:1542–1555. https://doi.org/10.1021/ct200909j.

80. Salomon-Ferrer, R., A. W. Götz, …, R. C. Walker. 2013. Routine microsecond molecular dynamics simulations with AMBER on GPUs. 2. Explicit solvent particle mesh Ewald. *J. Chem. Theory Comput.* 9:3878–3888. https://doi.org/10.1021/ct400314y.

81. Phillips, J. C., R. Braun, …, K. Schulten. 2005. Scalable molecular dynamics with NAMD. *J. Comput. Chem.* 26:1781–1802. https://doi.org/10.1002/jcc.20289.

82. Phillips, J. C., D. J. Hardy, …, E. Tajkhorshid. 2020. Scalable molecular dynamics on CPU and GPU architectures with NAMD. *J. Chem. Phys.* 153:044130. https://doi.org/10.1063/5.0014475.

83. Davidchack, R. L., R. Handel, and M. V. Tretyakov. 2009. Langevin thermostat for rigid body dynamics. *J. Chem. Phys.* 130:234101. https://doi.org/10.1063/1.3149788.

84. Darden, T., D. York, and L. Pedersen. 1993. Particle mesh Ewald: an N log (N) method for Ewald sums in large systems. *J. Chem. Phys.* 98:10089–10092. https://doi.org/10.1063/1.464397.

85. Scherer, M. K., B. Trendelkamp-Schroer, …, F. Noé. 2015. PyEMMA 2: a software package for estimation, validation, and analysis of Markov models. *J. Chem. Theory Comput.* 11:5525–5542. https://doi.org/10.1021/acs.jctc.5b00743.

86. Roe, D. R., and T. E. Cheatham. 2013. PTRAJ and CPPTRAJ: software for processing and analysis of molecular dynamics trajectory data. *J. Chem. Theory Comput.* 9:3084–3095. https://doi.org/10.1021/ct400341p.

87. Humphrey, W., A. Dalke, and K. Schulten. 1996. VMD: visual molecular dynamics. *J. Mol. Graph.* 14:33–38. https://doi.org/10.1016/0263-7855(96)00018-5.

88. Stone, J. 1998. *An Efficient Library for Parallel Ray Tracing and Animation*. Master's Thesis. Computer Science Department, University of Missouri-Rolla.

89. Schrödinger, L. L. C.. The PyMOL molecular graphics system. https://pymol.org/2/.

90. McGibbon, R. T., K. A. Beauchamp, …, V. S. Pande. 2015. MDTraj: a modern open library for the analysis of molecular dynamics trajectories. *Biophys. J.* 109:1528–1532. https://doi.org/10.1016/j.bpj.2015.08.015.

91. Hunter, J. D. 2007. Matplotlib: a 2D graphics environment. *Comput. Sci. Eng.* 9:90–95. https://doi.org/10.1109/MCSE.2007.55.

92. Waskom, M. 2021. seaborn: statistical data visualization. *J. Open Source Softw.* 6:3021. https://doi.org/10.21105/joss.03021.

93. Harris, C. R., K. J. Millman, …, T. E. Oliphant. 2020. Array programming with NumPy. *Nature.* 585:357–362. https://doi.org/10.1038/s41586-020-2649-2.

94. Getcontacts. https://getcontacts.github.io/.

95. Smart, O. S., J. M. Goodfellow, and B. A. Wallace. 1993. The pore dimensions of gramicidin A. *Biophys. J.* 65:2455–2460. https://doi.org/10.1016/s0006-3495(93)81293-1.

96. Hernández, C. X., and V. S. Pande. 2015. mdentropy: v0.2.https://doi.org/10.5281/zenodo.18859.

97. Lee, S., A. K. Nivedha, …, N. Vaidehi. 2019. Dynamic role of the G protein in stabilizing the active state of the adenosine A2A receptor. *Structure.* 27:703–712.e3. https://doi.org/10.1016/j.str.2018.12.007.

98. Bhattacharya, S., and N. Vaidehi. 2014. Differences in allosteric communication pipelines in the inactive and active states of a GPCR. *Biophys. J.* 107:422–434. https://doi.org/10.1016/j.bpj.2014.06.015.

99. Niesen, M. J. M., S. Bhattacharya, …, N. Vaidehi. 2013. Thermostabilization of the β1-adrenergic receptor correlates with increased entropy of the inactive state. *J. Phys. Chem. B.* 117:7283–7291. https://doi.org/10.1021/jp403207c.

100. Pandini, A., A. Fornili, …, J. Kleinjung. 2012. Detection of allosteric signal transmission by information-theoretic analysis of protein dynamics. *FASEB. J.* 26:868–881. https://doi.org/10.1096/fj.11-190868.

101. Dijkstra, E. W. 1959. A note on two problems in connexion with graphs. *Numer. Math.* 1:269–271. https://doi.org/10.1007/BF01386390.

102. Hagberg, A. A., D. A. Schult, and P. J. Swart. 2008. Exploring network structure, dynamics, and function using NetworkX. *In* Proceedings of the 7th Python in Science Conference G. Varoquaux, T. Vaught, and J. Millman, eds., pp. 11–15.

103. Bowman, G. R., D. L. Ensign, and V. S. Pande. 2010. Enhanced modeling via network theory: adaptive sampling of Markov state models. *J. Chem. Theory Comput.* 6:787–794. https://doi.org/10.1021/ct900620b.

104. Pérez-Hernández, G., F. Paul, …, F. Noé. 2013. Identification of slow molecular order parameters for Markov model construction. *J. Chem. Phys.* 139:015102. https://doi.org/10.1063/1.4811489.

105. Schwantes, C. R., and V. S. Pande. 2013. Improvements in Markov state model construction reveal many non-native interactions in the folding of NTL9. *J. Chem. Theory Comput.* 9:2000. https://doi.org/10.1021/ct300878a.

106. Turku, A., H. Schihada, …, G. Schulte. 2021. Residue 6.43 defines receptor function in class F GPCRs. *Nat. Commun.* 12:3919. https://doi.org/10.1038/s41467-021-24004-z.

107. Xu, L., B. Chen, H. Schihada, …, F. Xu. 2021. Cryo-EM structure of constitutively active human Frizzled 7 in complex with heterotrimeric Gs. *Cell Res.* 31:1311–1314. https://doi.org/10.1038/s41422-021-00525-6.

108. Hofmann, K. P., P. Scheerer, …, O. P. Ernst. 2009. A G protein-coupled receptor at work: the rhodopsin model. *Trends Biochem. Sci.* 34:540–552. https://doi.org/10.1016/j.tibs.2009.07.005.

109. Dijkgraaf, G. J. P., B. Alicke, …, F. J. de Sauvage. 2011. Small molecule inhibition of GDC-0449 refractory smoothened mutants and downstream mechanisms of drug resistance. *Cancer Res.* 71:435–444. https://doi.org/10.1158/0008-5472.can-10-2876.

110. Huang, P., S. Zheng, …, A. Salic. 2018. Structural basis of smoothened activation in hedgehog signaling. *Cell.* 174:312–324.e16. https://doi.org/10.1016/j.cell.2018.04.029.

111. Myers, B. R., N. Sever, …, P. A. Beachy. 2013. Hedgehog pathway modulation by multiple lipid binding sites on the smoothened effector of signal response. *Dev. Cell.* 26:346–357. https://doi.org/10.1016/j.devcel.2013.07.015.

112. Yang, H., J. Xiang, …, S. Lin. 2009. Converse conformational control of smoothened activity by structurally related small molecules. *J. Biol. Chem.* 284:20876–20884. https://doi.org/10.1074/jbc.m807648200.

113. Hedger, G., H. Koldsø, …, M. S. P. Sansom. 2019. Cholesterol interaction sites on the transmembrane domain of the hedgehog signal transducer and class F G protein-coupled receptor smoothened. *Structure.* 27:549. https://doi.org/10.1016/j.str.2018.11.003.

114. Cherezov, V., D. M. Rosenbaum, …, R. C. Stevens. 2007. High-resolution crystal structure of an engineered human β2-adrenergic G protein–coupled receptor. *Science.* 318:1258–1265. https://doi.org/10.1126/science.1150577.

115. Rasmussen, S. G. F., H.-J. Choi, …, B. K. Kobilka. 2011. Structure of a nanobody-stabilized active state of the β2 adrenoceptor. *Nature.* 469:175–180. https://doi.org/10.1038/nature09648.

116. Robert, X., and P. Gouet. 2014. Deciphering key features in protein structures with the new ENDscript server. *Nucleic Acids Res.* 42:W320. https://doi.org/10.1093/nar/gku316.

117. ESPript, 'easy sequencing in PostScript'. https://espript.ibcp.fr/ESPript/ESPript/index.php.

Biophysical Journal, Volume *122*

Supplemental information

Activation mechanism of the human Smoothened receptor

Prateek D. Bansal, Soumajit Dutta, and Diwakar Shukla

Manuscript submitted to **Biophysical***Journal*
Article

Activation mechanism of the human Smoothened receptor

Prateek D. Bansal[1], Soumajit Dutta[1], and Diwakar Shukla[1,2,3,4*]

[1]Department of Chemical and Biomolecular Engineering, University of Illinois at Urbana-Champaign, Urbana, IL, 61801, United States
[2]Department of Bioengineering, University of Illinois at Urbana-Champaign, Urbana, IL, 61801, United States
[3]Center for Biophysics and Quantitative Biology, University of Illinois at Urbana-Champaign, Urbana, IL, 61801, United States
[4]Cancer Center at Illinois, University of Illinois at Urbana-Champaign, Urbana, IL, 61801, United States
[*]Correspondence: diwakar@illinois.edu

SUPPLEMENTARY FIGURES

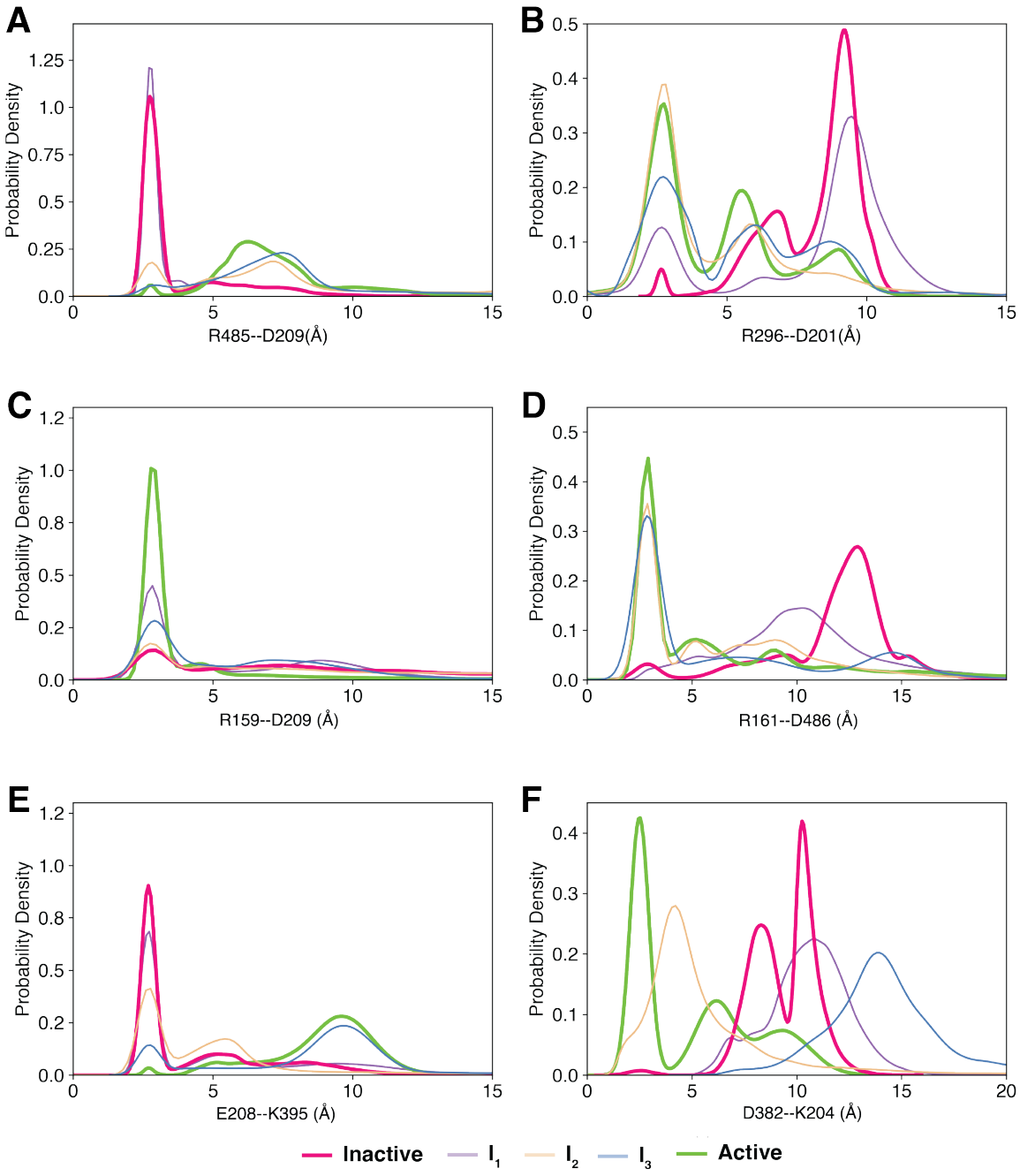

Figure S1: Figure 3 reconstructed using CHARMM36m force field. Use of CHARMM36m force field made noted no significant difference to the overall observations made using CHARMM36 force field.

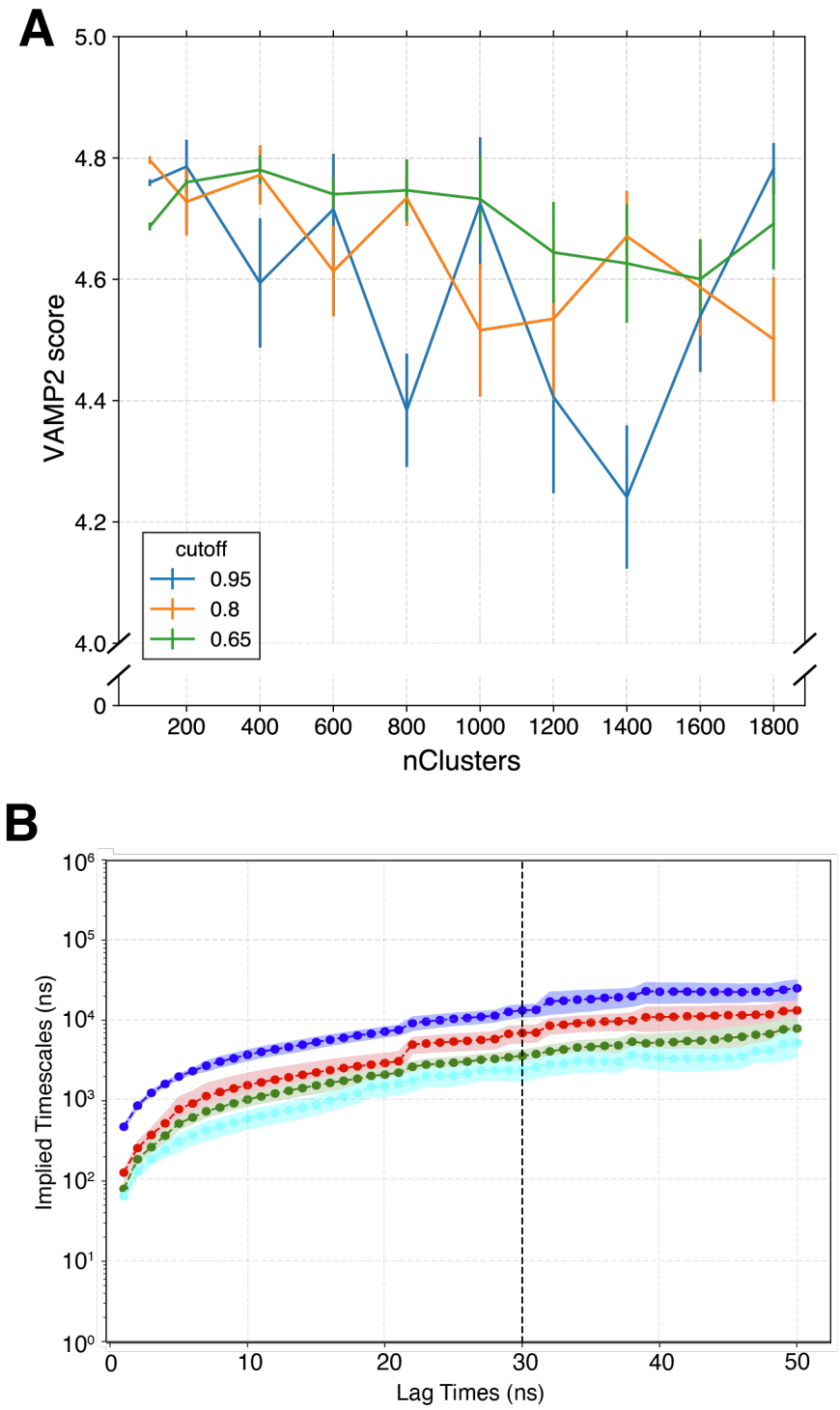

Figure S2: MSM construction for Apo-SMO. (A) VAMP2 score v/s nClusters used to cluster the data, as a function of varying variational cutoffs for choosing the number of tICA (time Independent Component Analysis) components. For final MSM construction, 200 clusters with a 0.95 variational cutoff (corresponding to 42 tICA components) was chosen to construct the MSM. (B) Implied Timescales v/s MSM lag time for the MSM with 200 clusters and 42 tICA components. A lagtime of 30 ns was chosen for construction of the final MSM.

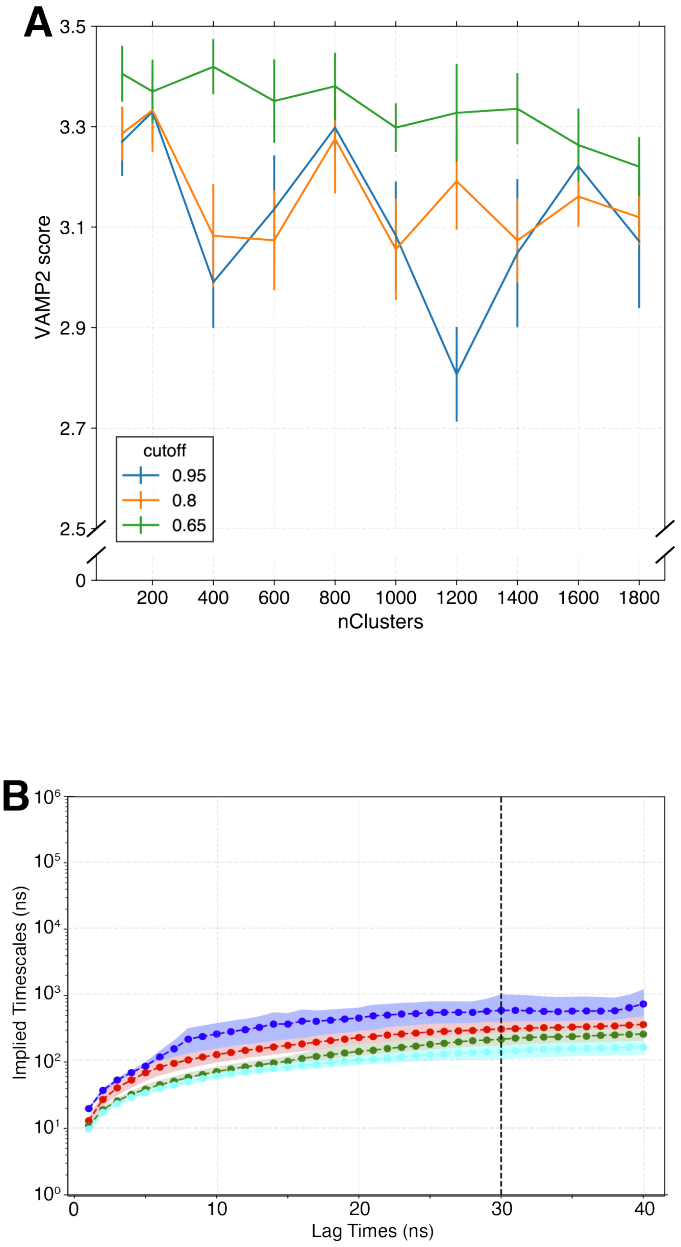

Figure S3: MSM construction for SANT1-SMO. (A) VAMP2 score v/s nClusters used to cluster the data, as a function of varying variational cutoffs for choosing the number of tICA (time Independent Component Analysis) components. For final MSM construction, 100 clusters with a 0.95 variational cutoff (corresponding to 34 tICA components) was chosen to construct the MSM. (B) Implied Timescales v/s MSM lag time for the MSM with 100 clusters and 34 tICA components. A lagtime of 30 ns was chosen for construction of the final MSM.

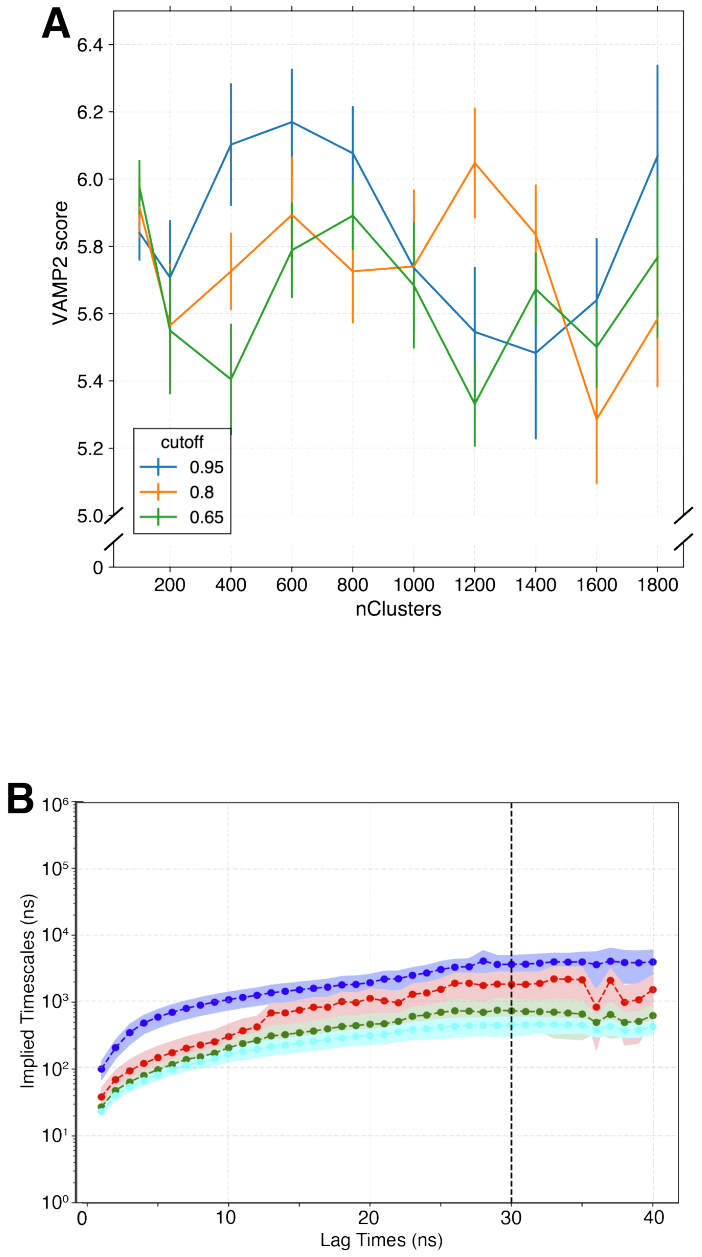

Figure S4: MSM construction for SAG-SMO. (A) VAMP2 score v/s nClusters used to cluster the data, as a function of varying variational cutoffs for choosing the number of tICA (time Independent Component Analysis) components. For final MSM construction, 100 clusters with a 0.95 variational cutoff (corresponding to 34 tICA components) was chosen to construct the MSM. (B) Implied Timescales v/s MSM lag time for the MSM with 100 clusters and 34 tICA components. A lagtime of 30 ns was chosen for construction of the final MSM.

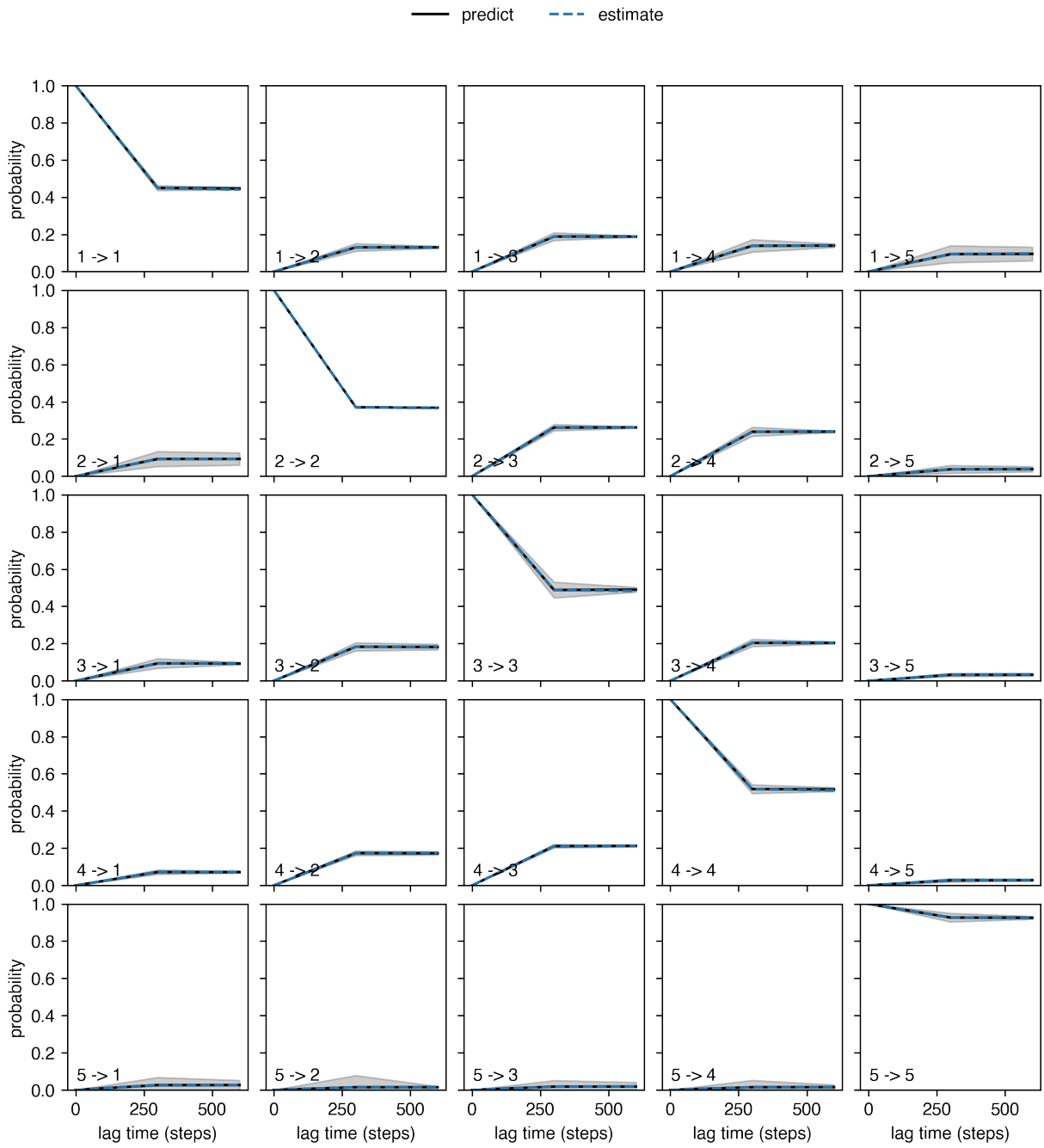

Figure S5: MSM validation for Apo-SMO. Chapman-Kolmogorov test performed for 5 macrostates for Apo-SMO. Chapman-Kolmogorov test was implemented using the pyEMMA package.(1)

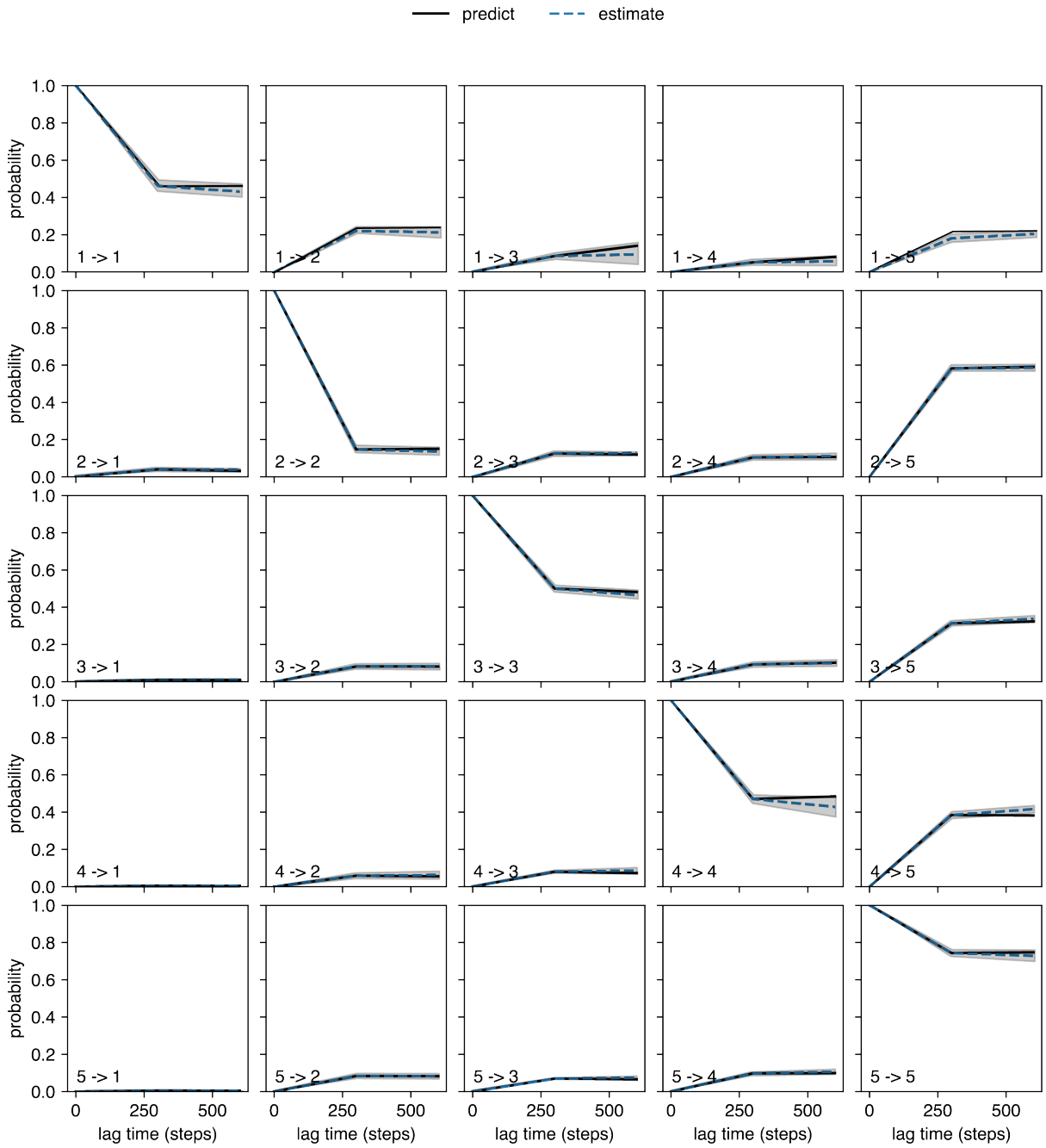

Figure S6: MSM validation for SANT1-SMO. Chapman-Kolmogorov test performed for 5 macrostates for SANT1-SMO. Chapman-Kolmogorov test was implemented using the pyEMMA package.(1)

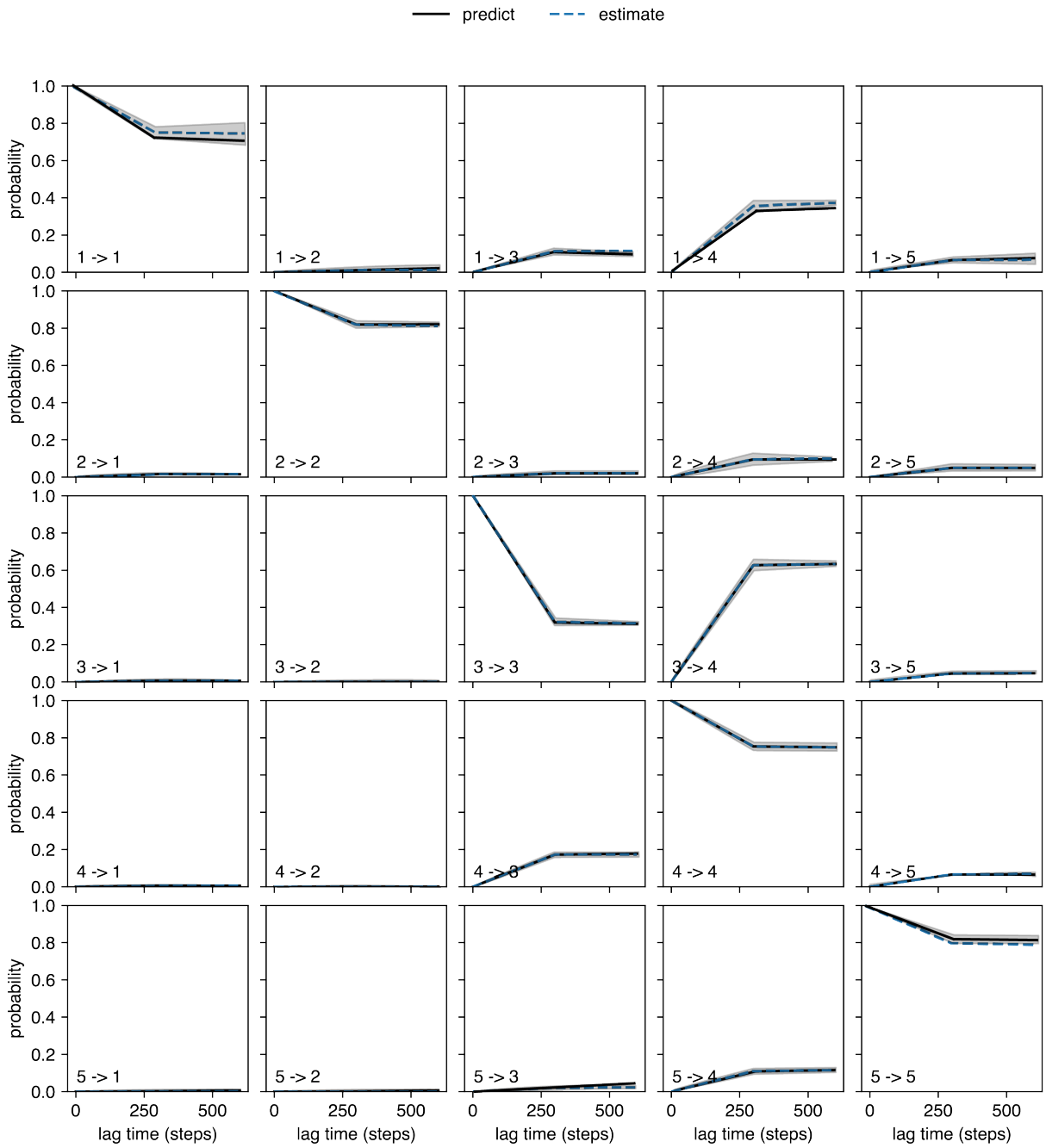

Figure S7: MSM validation for SAG-SMO. Chapman-Kolmogorov test performed for 5 macrostates for SAG-SMO. Chapman-Kolmogorov test was implemented using the pyEMMA package.(1)

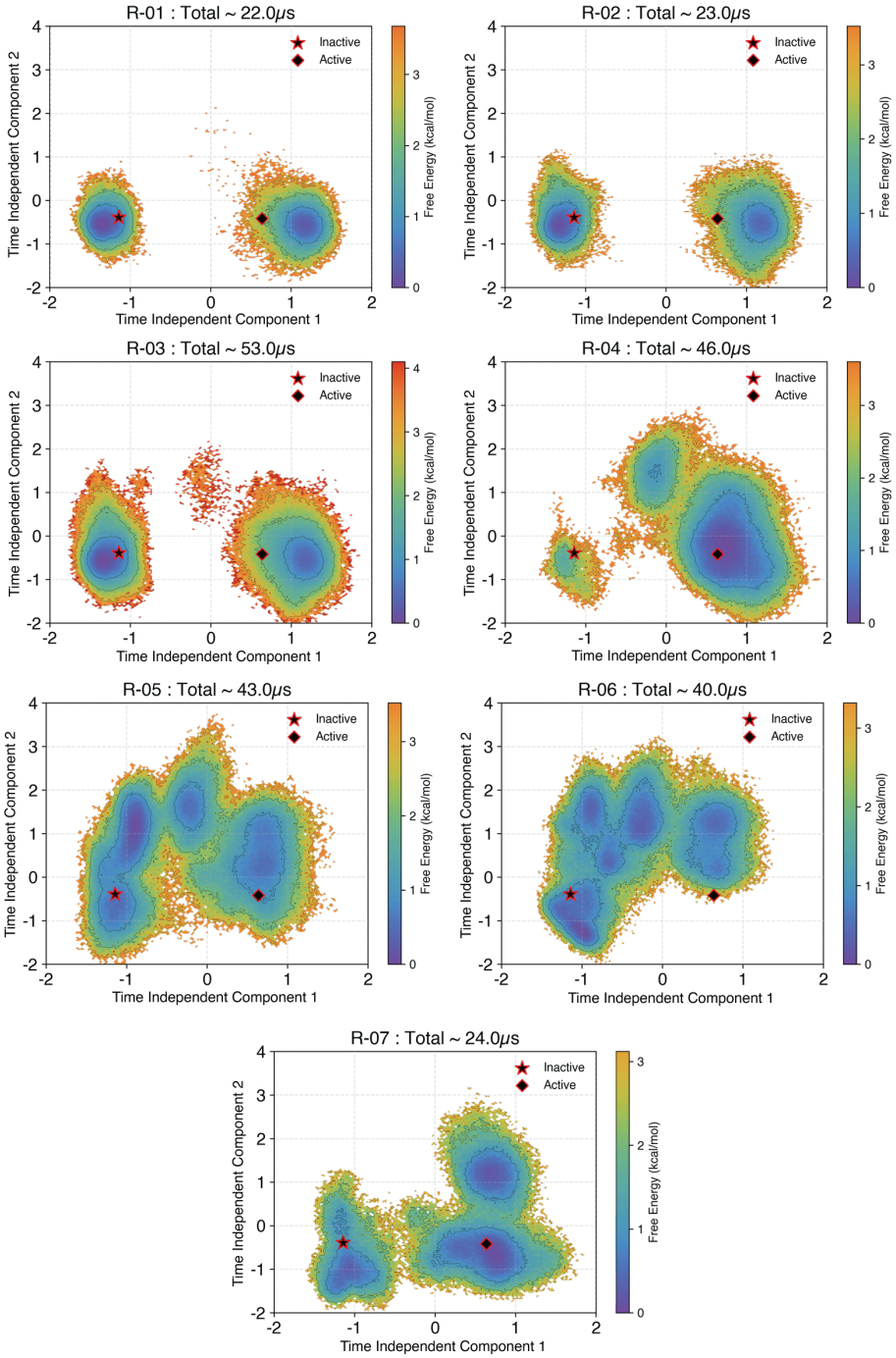

Figure S8: Roundwise data collection for adaptive sampling in Apo-SMO. The 2 startpoints and amount of data collected in that round are mentioned on each plot. A total of 7 rounds of sampling was performed.

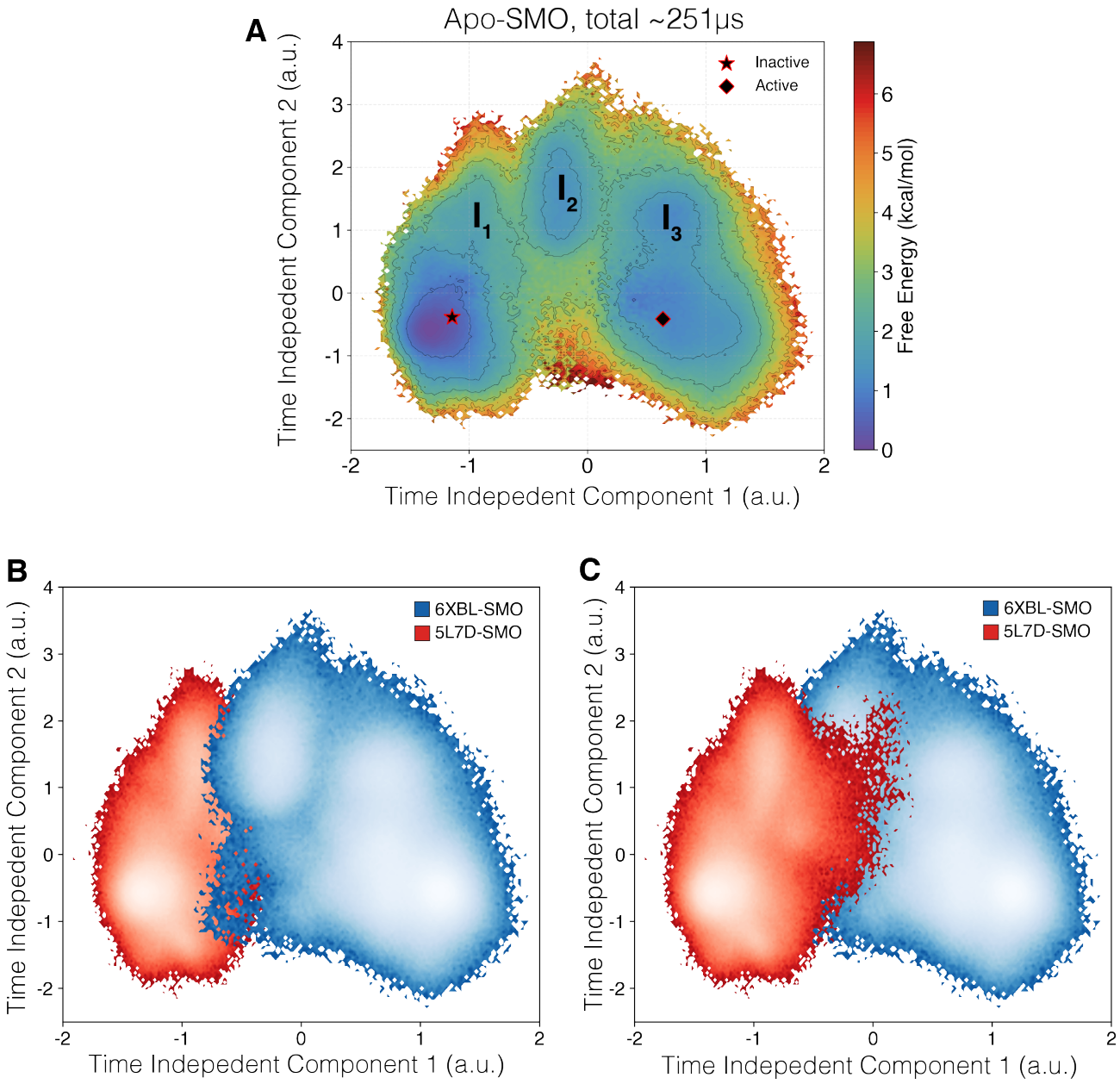

Figure S9: Apo-SMO tICA plots outlining the slowest processes. (A) Projection of MSM weighted simulation data for Apo-SMO on the tICA space, using the 2 slowest components. The inactive and active starting points are marked. The inactive and active starting points show a free energy difference of ~ 1 kcal.mol^{-1}. Intermediate states I_1, I_2 and I_3 are as marked. The intermediate states I_{1-3} were defined based on metastable basins and free energy barriers associated with transitioning from an inactive to an active state. A cutoff of 1.8 kcal/mol was used to separate one basin from another. (B,C) Projection of the data for each starting point shown separately on the tICA landscape. The two islands show overlap, indicating transitions that span the slowest component. Red denotes the data collected from the inactive starting structure, while Blue denotes the data collected from the active starting structure.

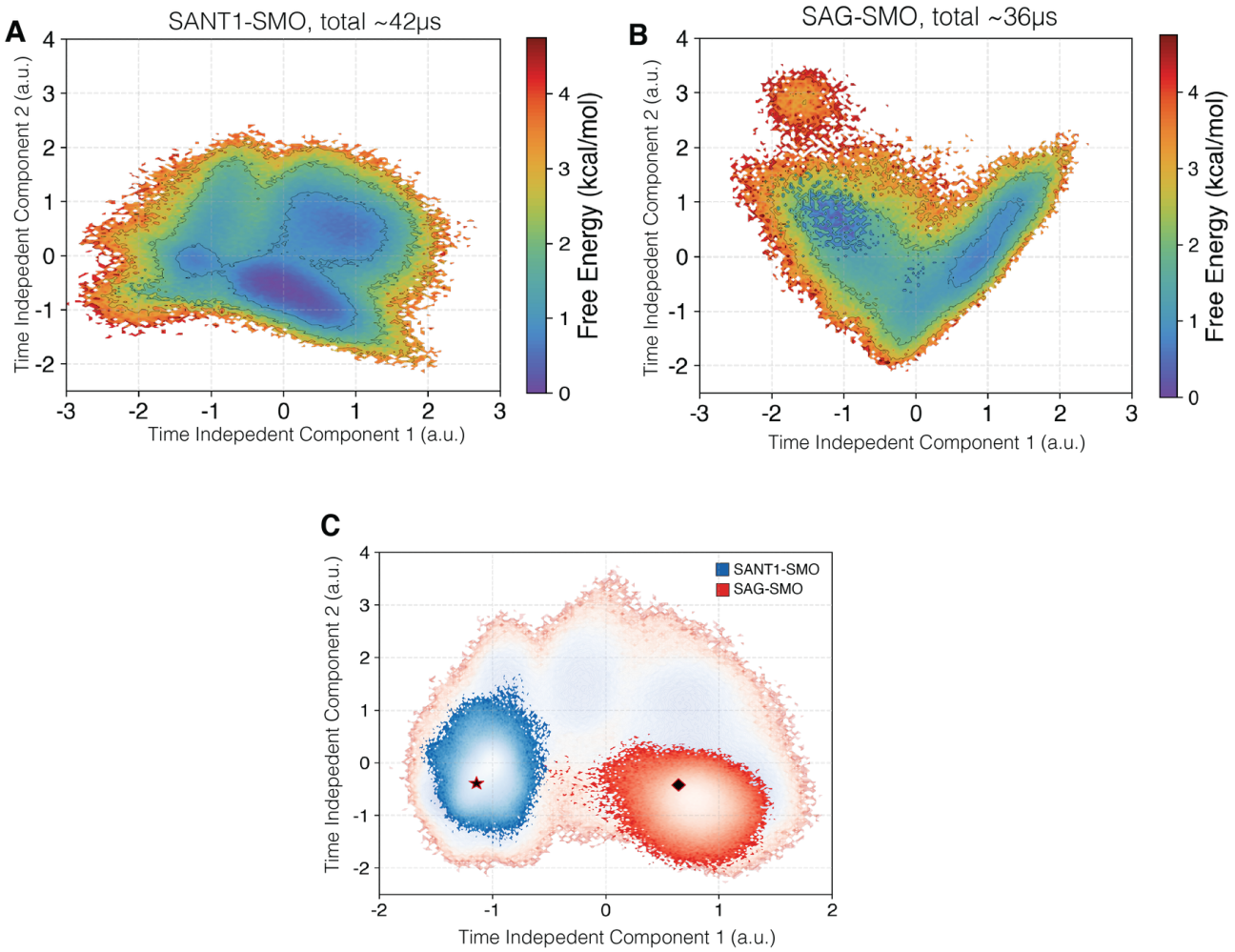

Figure S10: Projection of MSM weighted simulation data for (A) SANT1-SMO and (B) SAG-SMO on the tICA space, using the 2 slowest components. (C) The same data as (A) and (B), when projected on the tICA space defined by Apo-SMO. The inactive and active structures are marked as star and diamond, respectively.

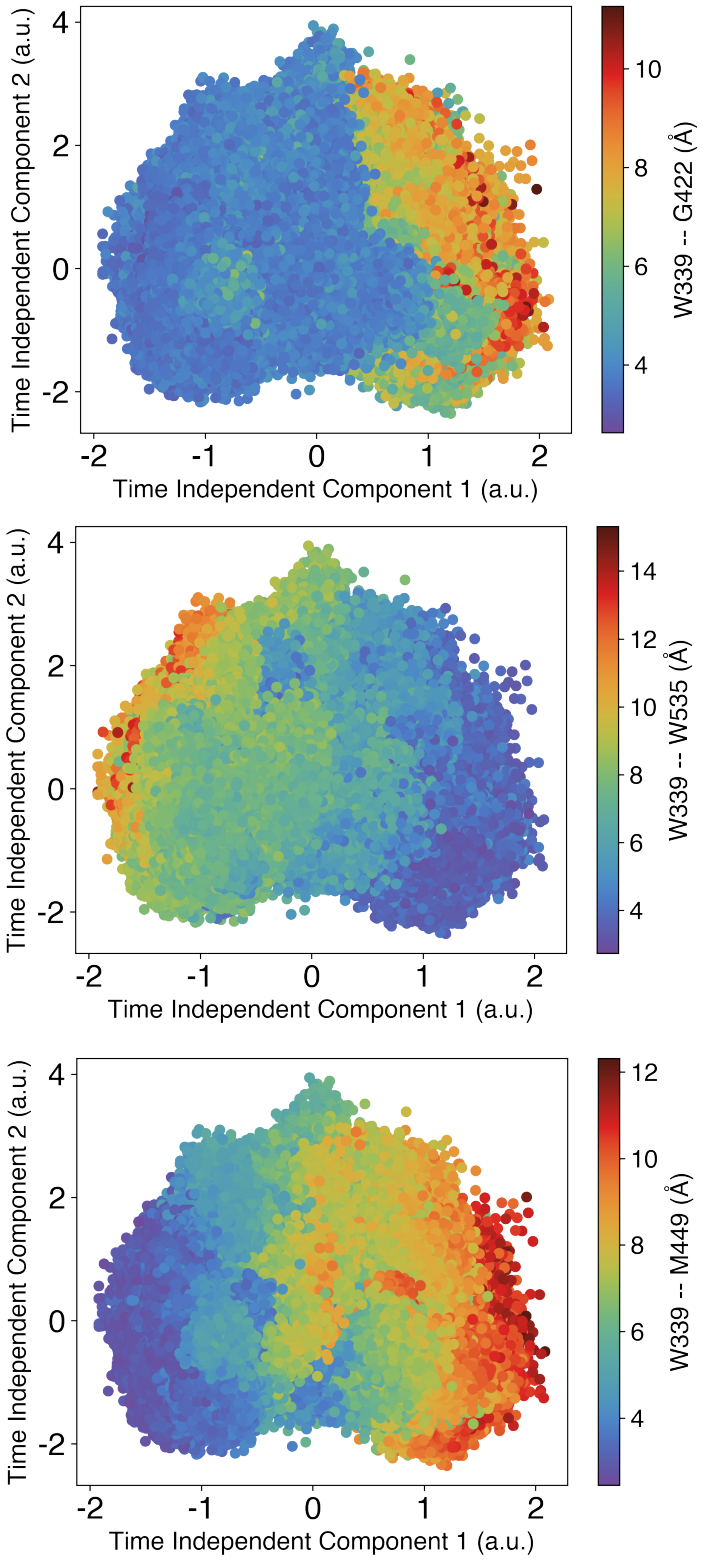

Figure S11: TICA Scatterplots show residue-correlated movements with activation on tICA space. Scatterplots showing the correlation of the intracellular residue distances W339-G422 (TM3-TM5), W339-W535 (Ionic Lock) and W339-M449 (TM3 - TM6), projected on the tICA landscape. tIC1 corresponds to SMO activation, hence these distances are integral to SMO activation.

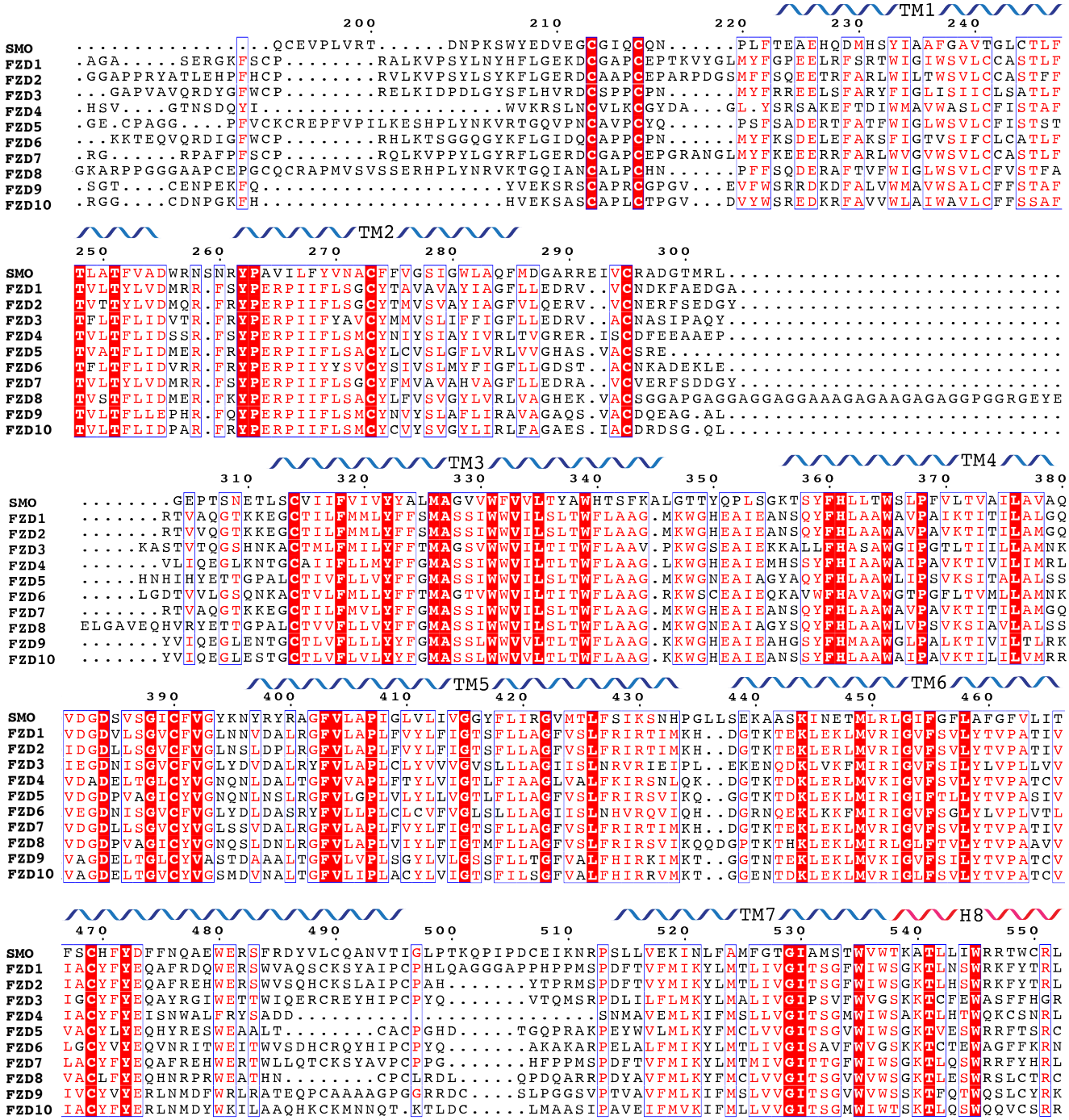

Figure S12: Multiple Sequence Alignment of Class F receptor Transmembrane Domains. Residues highlighted in red are conserved across the entire family.

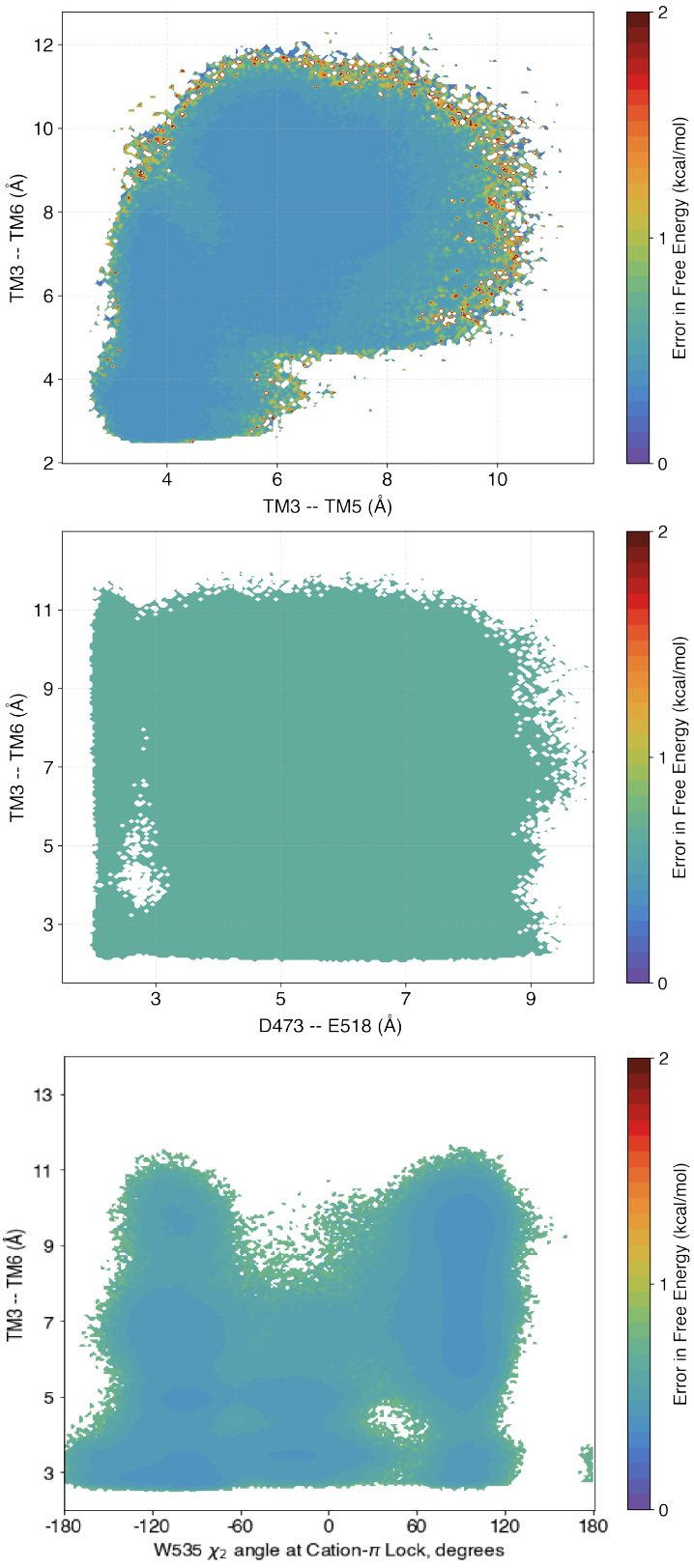

Figure S13: Error in the free-energy plots discussed in Fig 2 of the main text. Errors calculated using bootstrapping - 80% of the data was used in 200 iterations to produce the error.

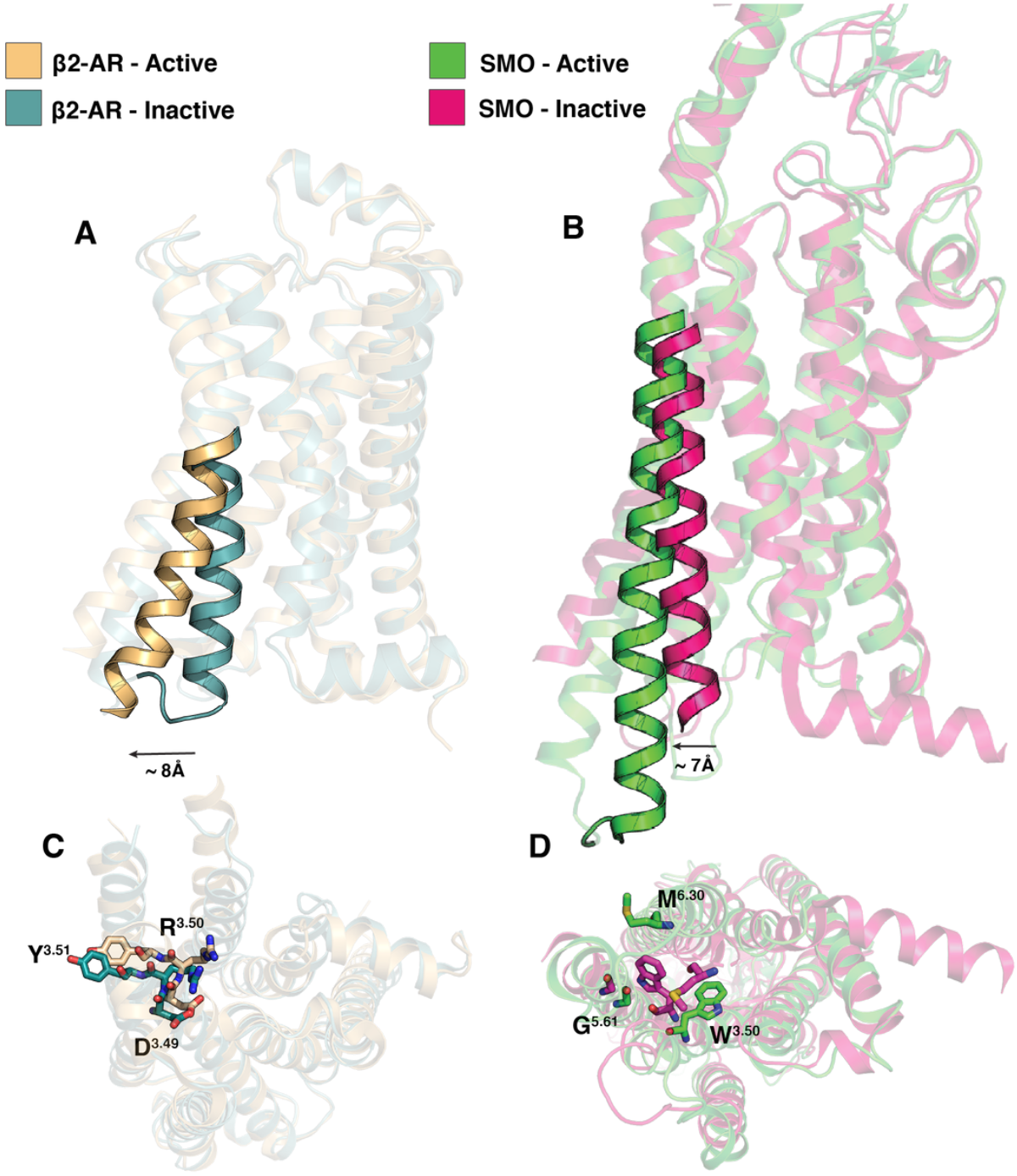

Figure S14: Qualitative comparison in the structural commonalities between Class A and Class F GPCRs. β_2-AR (A), a class A GPCR, shows the canonical outward movement of TM6 corresponding to receptor activation (2, 3). SMO (B) also shows the corresponding outward movement. (C,D) Intracellular view of the D-R-Y (C) and W-G-M (D) motifs.

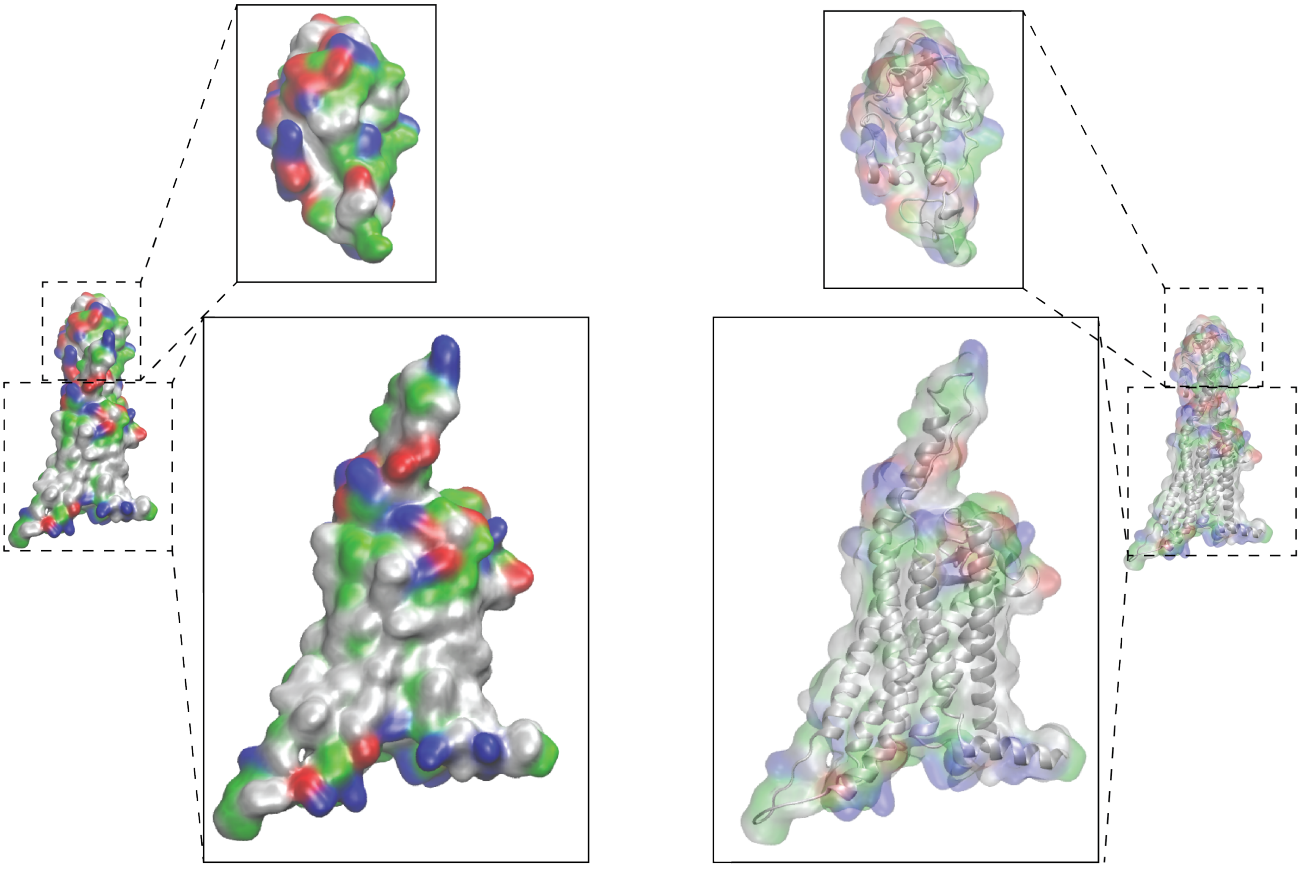

Figure S15: Difference in the polarity of residues between the CRD (top) vs TMD (bottom). Residues colored in red-blue are polar, while green-white residues show the hydrophobic residues.

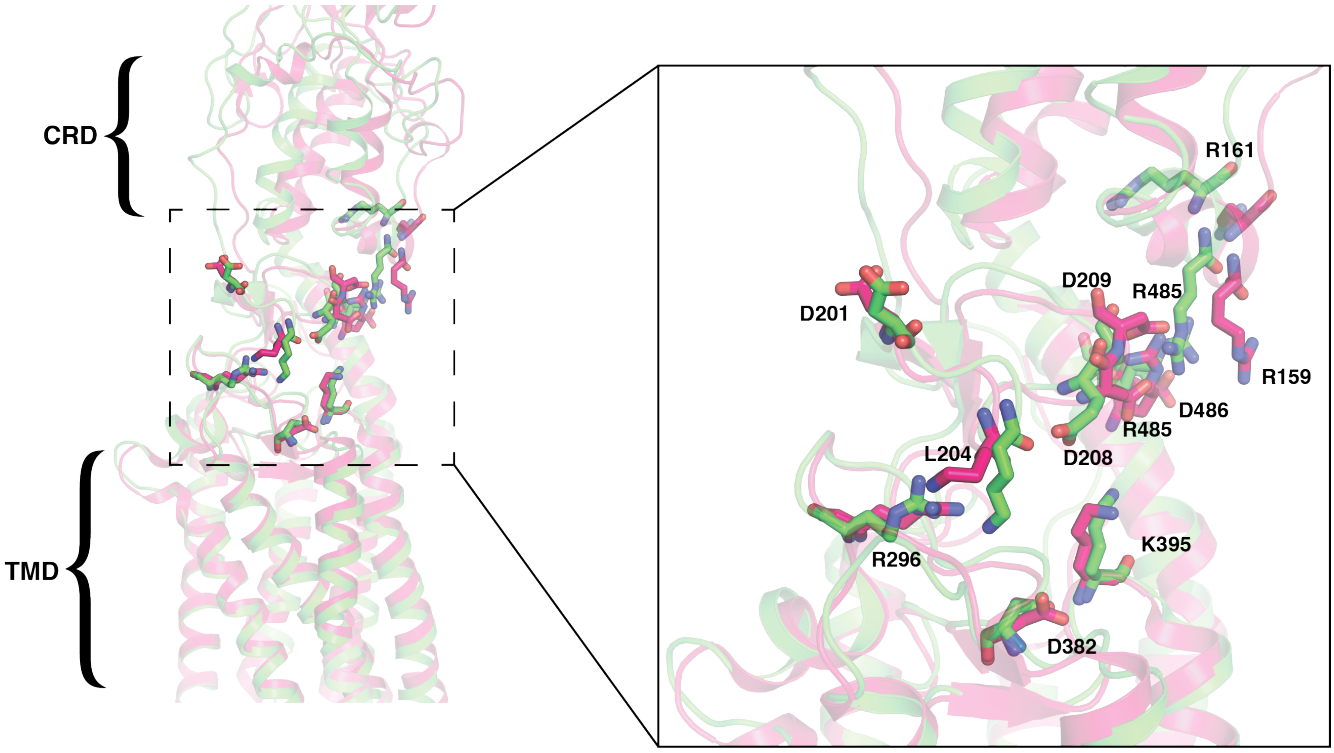

Figure S16: Rearrangement of the salt-bridges on the CRD-TMD interface. Inset shows the particular salt bridges involved in SMO activation.

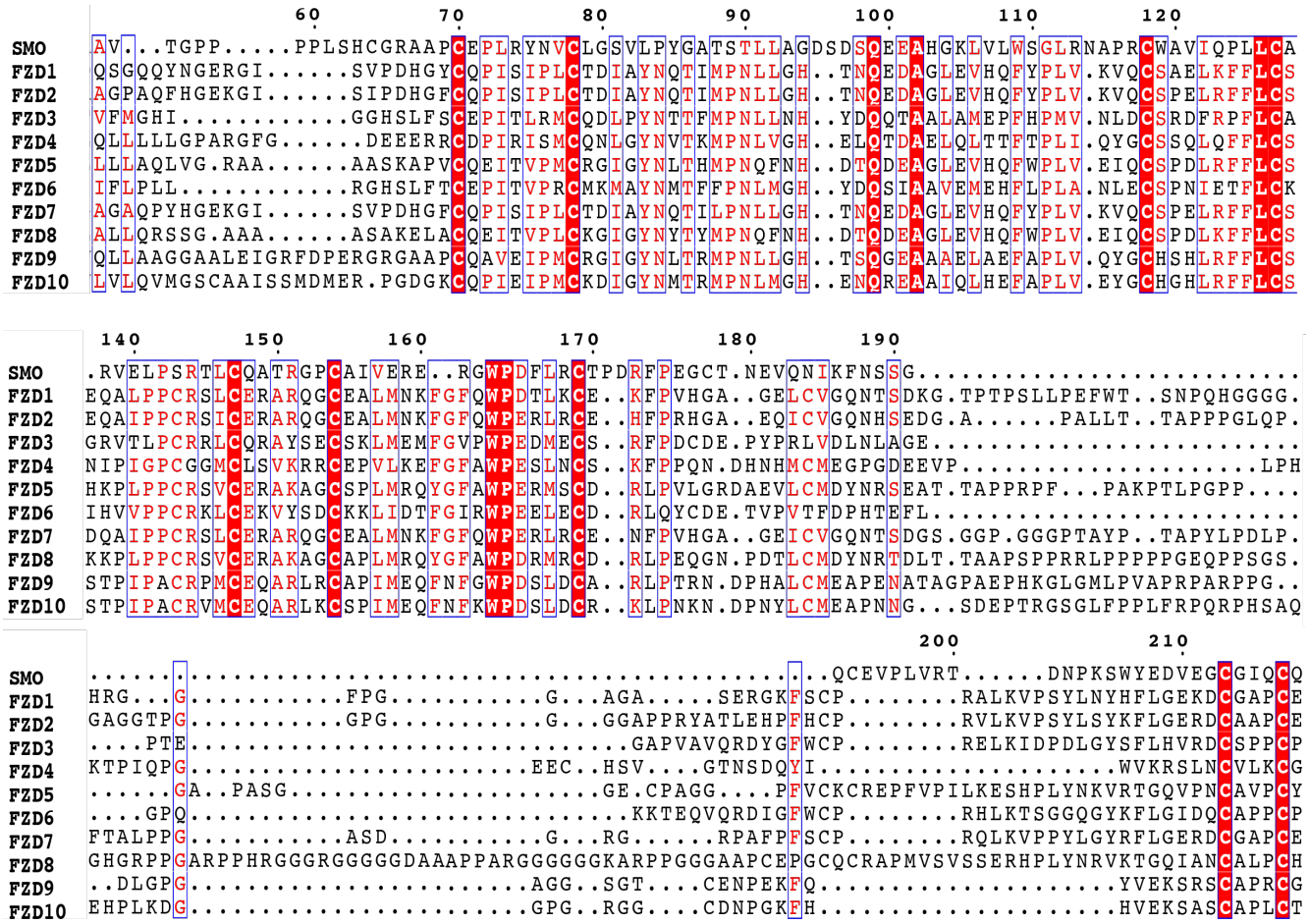

Figure S17: Multiple Sequence Alignment for the CRD of Class F receptors. The alignment was perfomed using ESPript3 web server(4, 5)

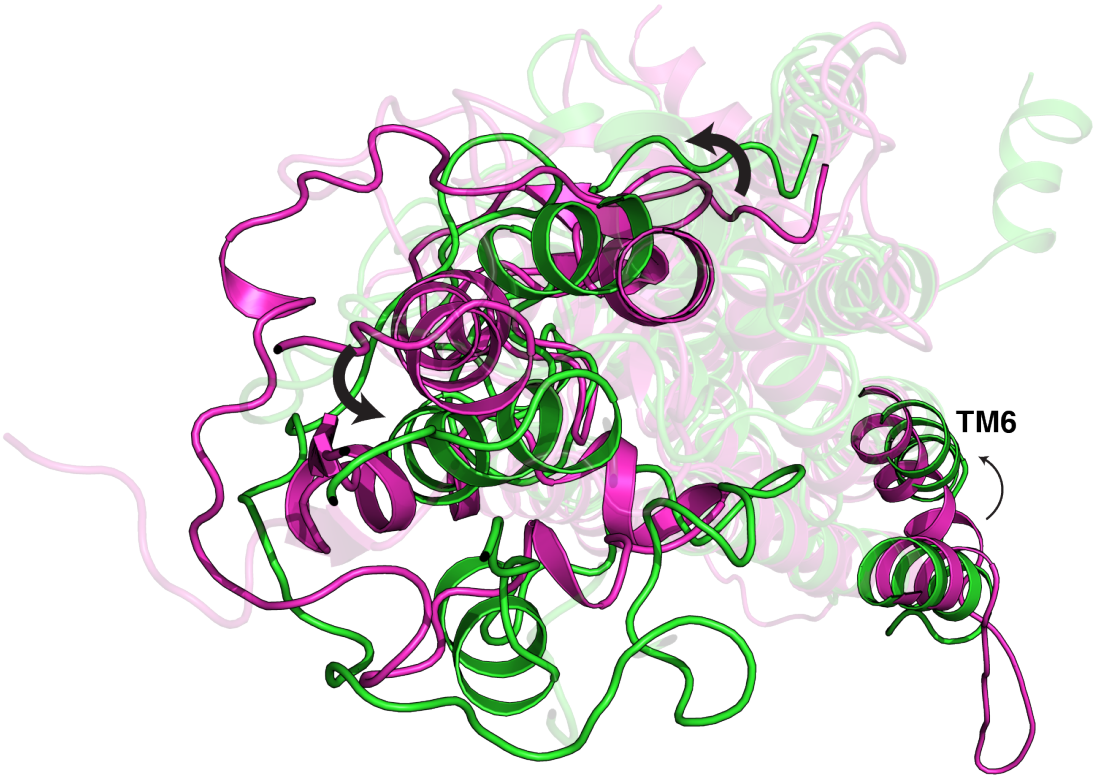

Figure S18: Rotation of CRD on activation. (Pink-Inactive SMO; Green-Active SMO) CRD undergoes a reorientation during SMO activation, which is characterized by the outward movement of TM6.

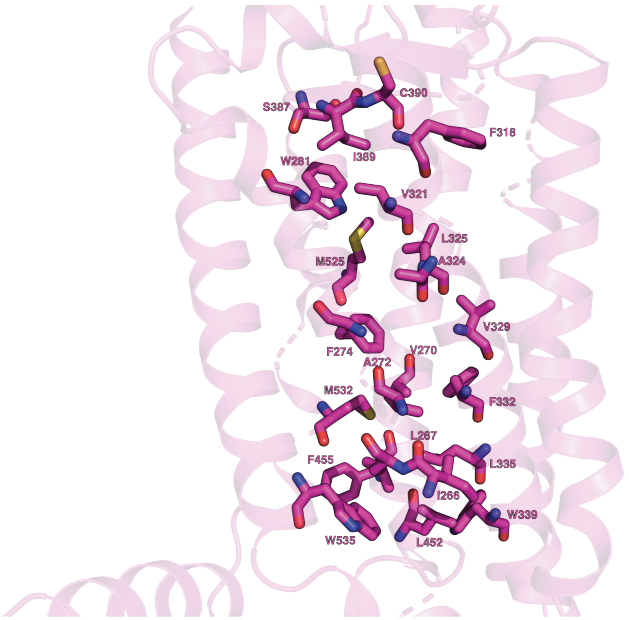

Figure S19: Hydrophobic tunnel inside SMO. The tunnel inside SMO consists of primarily hydrophobic residues, lining the tunnel from the extracellular end (top) to the intracellular end (bottom)

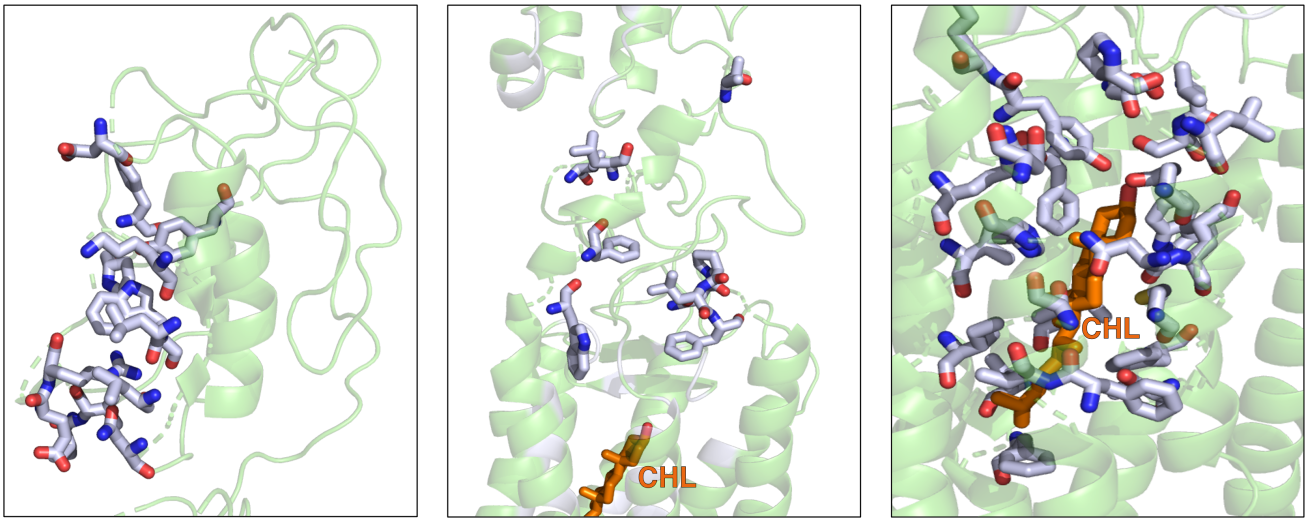

Figure S20: Pathway to the CRD for proposed cholesterol transport. Various residues line the pathway between the entry-point of cholesterol from the membrane to the binding site, in the CRD. These consist of residues close to the extracellular binding site in the ECD, in the linker domain (LD) which connects the CRD to the TMD, and in the core TM domain. The residues were determined based on the proximity of the sterol in multiple sterol-bound resolved structures of SMO (PDB ID 6XBL, 6XBM(6) and 5L7D(7).

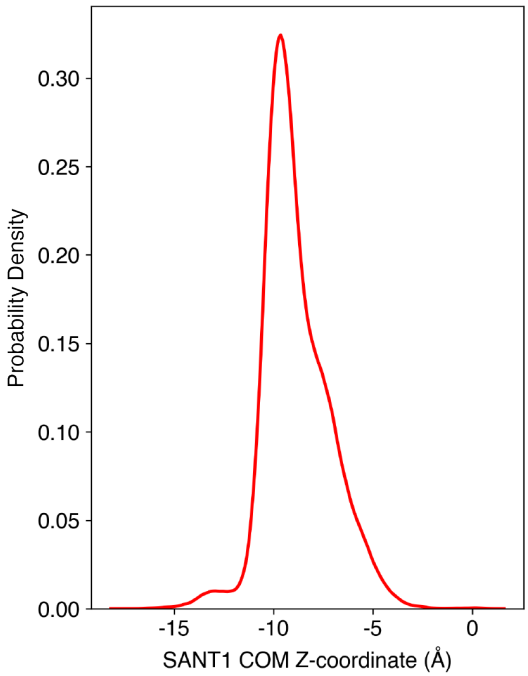

Figure S21: Lateral movement of SANT1 center of mass. Simulations show a minimal lateral movement of SANT1 across the hydrophobic tunnel, suggesting that SANT1 operates as an antagonist by sterically blocking the tunnel.

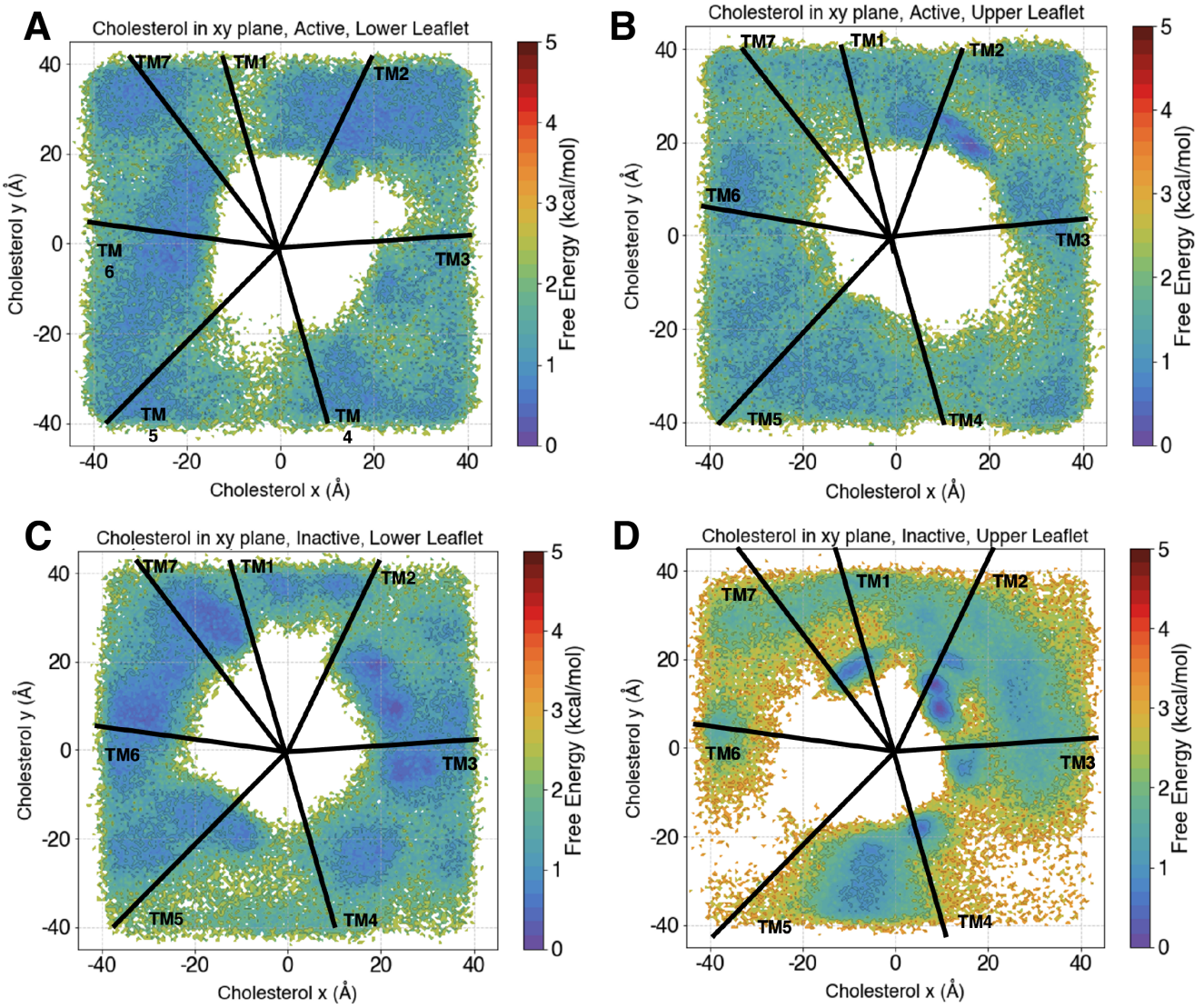

Figure S22: Observed cholesterol densities in the membrane during Apo-SMO simulations. The plots show the distribution of the cholesterol in the membrane, with the white space in the middle occupied by SMO. (A-C) Cholesterol shows a uniform distribution in the Lower leaflet regardless of the conformation, as well as the upper leaflet in the active state. (D) Cholesterol, however, does show a propensity to cluster outside the area between TM2 and TM3 in the upper leaflet, showing a conformational dependence on the cholesterol distribution. The black lines show the average position of the helix in the membrane as seen from above, looking directly into the core of the protein.

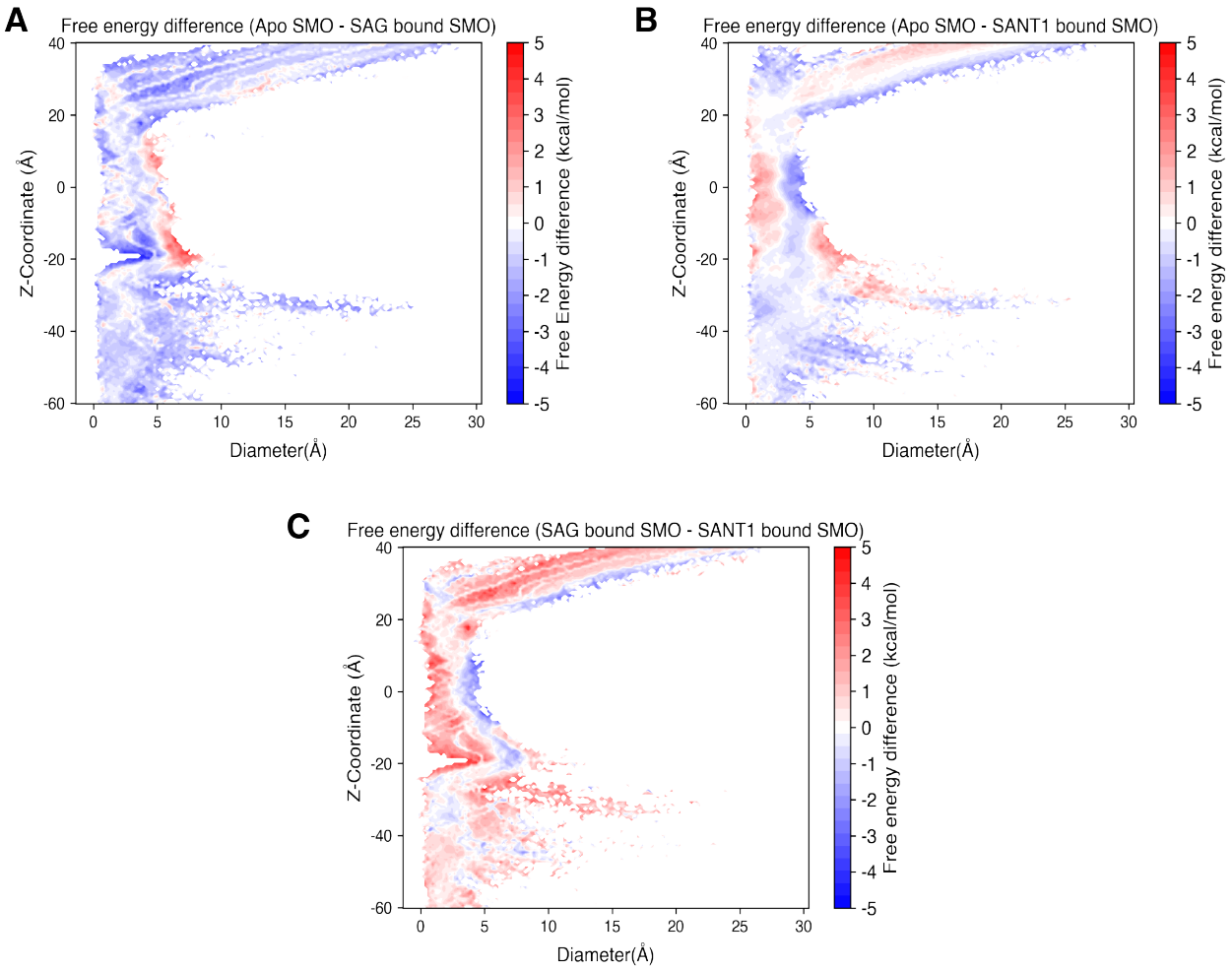

Figure S23: Free energy difference between the various plots shown in Fig 5. Z-coordinate vs tunnel diameter free energy differences were plotted between (A) - Apo-SMO and SAG bound SMO, (B) Apo-SMO and SANT1 bound SMO, and (C) SAG-bound SMO and SANT1-bound SMO.

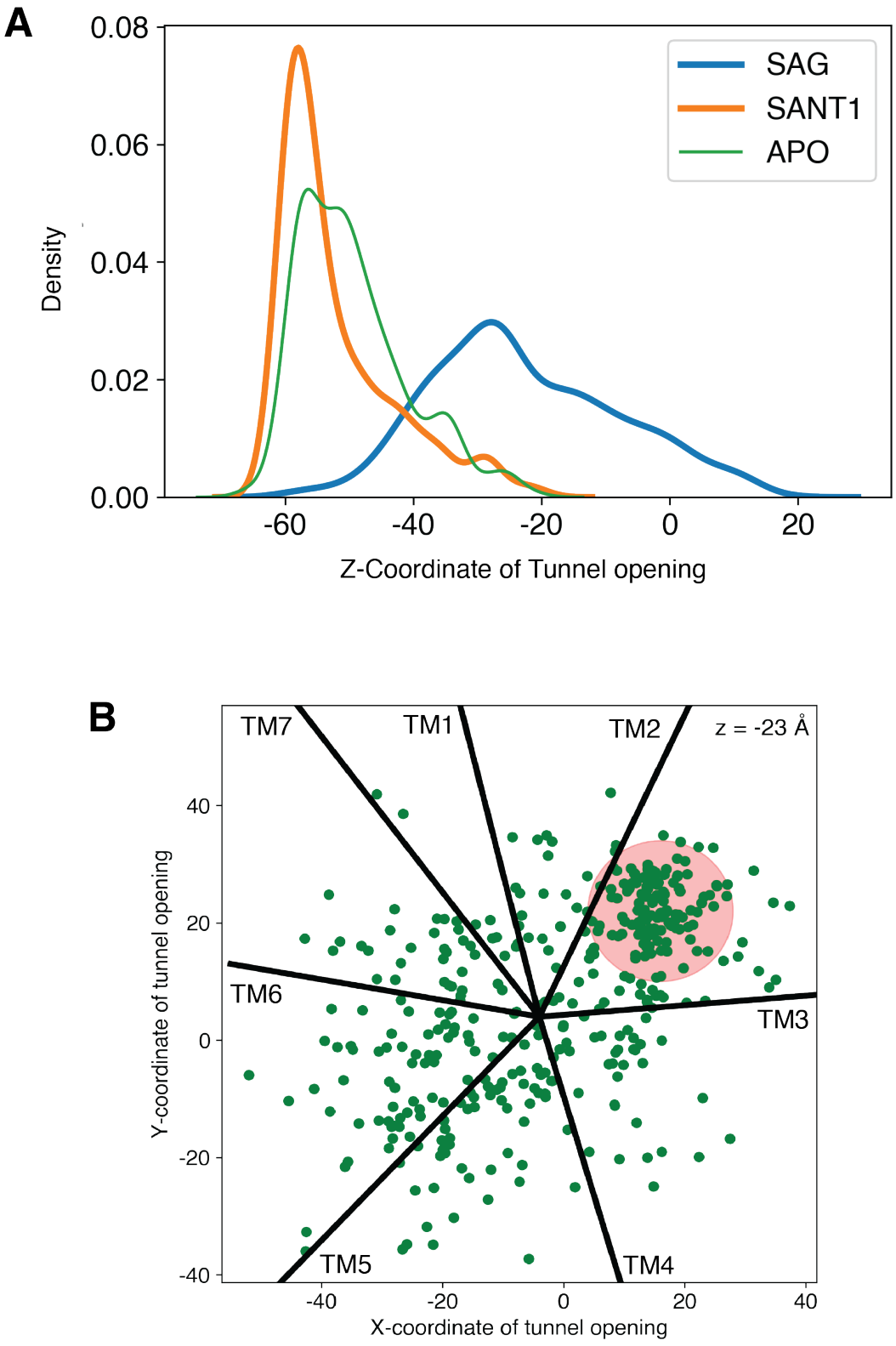

Figure S24: (A) Probability density of Z-coordinate of tunnel opening. Simulations show that the tunnel opens in the upper leaflet of the membrane, z ~ -22. (B) The Y v/s X coordinate (Z = -23) of tunnel opening in SAG-SMO. A cluster is centered around the interface of TM2 and TM3, circled in red. The various helical boundaries are shown using black lines.

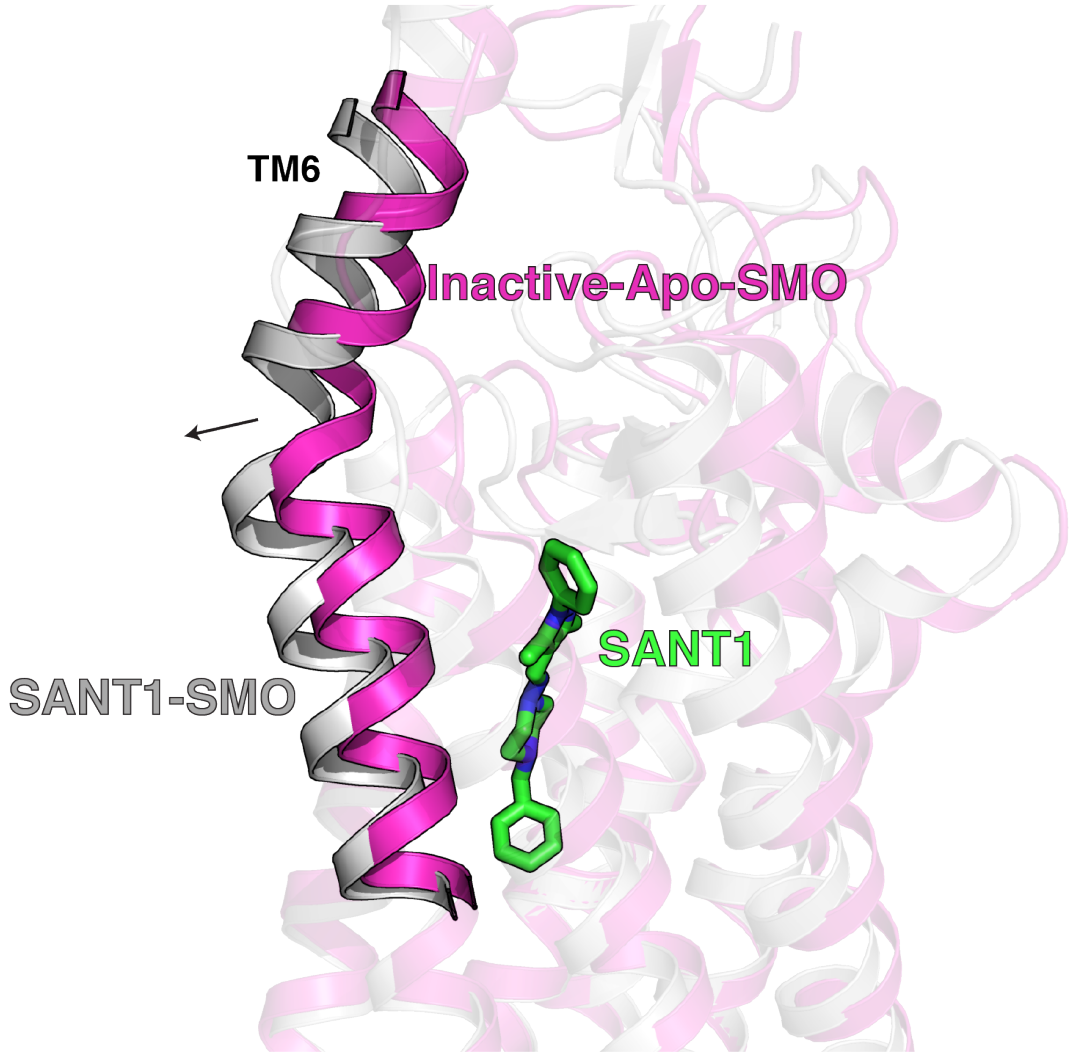

Figure S25: Helical displacement of TM6 by SANT1. This helical displacement causes the shift in the allosteric network of SMO, precluding the transition to active state.

Simulation Round	Amount of Apo-SMO-Data
Round 1	22μs
Round 2	23μs
Round 3	53μs
Round 4	46μs
Round 5	43μs
Round 6	40μs
Round 7	24μs
Total	251 μs

Table S1: Round wise data collection for Apo-SMO.

Simulation Round	Amount of SAG-SMO-Data	Amount of SANT1-SMO-Data
Round 1	10μs	10μs
Round 2	12μs	14μs
Round 3	14μs	18μs
Total	36 μs	42μs

Table S2: Round wise data collection for SAG-SMO and SANT1-SMO

Modelled Residues in 5L7D-inac-Apo-SMO	Constraints	Location
I429	None	ICL3
K430	None	ICL3
S431	None	ICL3
N432	None	ICL3
H433	None	ICL3
P434	None	ICL3
G435	None	ICL3
L436	None	ICL3
L437	None	ICL3
S438	None	ICL3
E439	None	ICL3
K440	α-helical	TM6
A441	α-helical	TM6
A442	α-helical	TM6
S443	α-helical	TM6
K444	α-helical	TM6
I445	α-helical	TM6

Table S3: Modelled residues in 5L7D-inactive-Apo-SMO starting structure. The helical content of K440-I445 was modelled based on the structure of SANT1-bound SMO (PDB: 4N4W) (8)

Lipid	Upper Leaflet	Lower Leaflet
Cholesterol	21	21
POPC	76	76
Sphingomyelin	4	4
Total	101	101

Table S4: Membrane composition used for simulations.

P58	P59	R66	R173	Y85	K133
L106	Y130	L108	W109	W109	L126
R113	W119	A115	E211	R117	W206
R117	G212	W119	Q123	Q123	F187
R151	W163	W163	R168	C169	F174
N202	W206	W206	E211	W206	G212
Y207	E208	Y207	D209	F222	L515
H231	F285	H231	R290	L246	F275
F252	S259	F252	F268	W256	F268
Y262	L353	Q284	R290	G288	E292
R290	R291	F332	A459	L335	W339
W339	G422	W339	M449	W339	G453
W339	W535	F343	M449	L346	I445
L353	F360	K356	F360	Q380	Y399
V381	V392	Y397	F474	Y397	Q477
L419	F457	H433	P434	H433	G435
G435	L436	S443	N446	H470	F474
W480	P513	Y487	Q491	Y487	I509
Q502	I504	L516	K519	T534	W537

Table S5: Adaptive Sampling metrics used for clustering in Apo-SMO, SANT1-SMO and SAG-SMO. Double lines separate pairs of residues.

REFERENCES

1. Scherer, M. K., B. Trendelkamp-Schroer, F. Paul, G. Pérez-Hernández, M. Hoffmann, N. Plattner, C. Wehmeyer, J.-H. Prinz, and F. Noé, 2015. PyEMMA 2: A Software Package for Estimation, Validation, and Analysis of Markov Models. *J. Chem. Theory Comput.* 11:5525–5542. doi:10.1021/acs.jctc.5b00743.

2. Cherezov, V., D. M. Rosenbaum, M. A. Hanson, S. G. F. Rasmussen, F. S. Thian, T. S. Kobilka, H.-J. Choi, P. Kuhn, W. I. Weis, B. K. Kobilka, and R. C. Stevens, 2007. High-Resolution Crystal Structure of an Engineered Human β2-Adrenergic G Protein–Coupled Receptor. *Science* 318:1258–1265. doi:10.1126/science.1150577.

3. Rasmussen, S. G. F., H.-J. Choi, J. J. Fung, E. Pardon, P. Casarosa, P. S. Chae, B. T. DeVree, D. M. Rosenbaum, F. S. Thian, T. S. Kobilka, A. Schnapp, I. Konetzki, R. K. Sunahara, S. H. Gellman, A. Pautsch, J. Steyaert, W. I. Weis, and B. K. Kobilka, 2011. Structure of a nanobody-stabilized active state of the β2 adrenoceptor. *Nature* 469:175–180. doi:10.1038/nature09648.

4. Robert, X., and P. Gouet, 2014. Deciphering key features in protein structures with the new ENDscript server. *Nucleic Acids Res.* 42:W320–W324. doi:10.1093/nar/gku316.

5. ESPript. 2022. January 15 2022. https://espript.ibcp.fr/ESPript/ESPript/index.php.

6. Qi, X., L. Friedberg, R. D. Bose-Boyd, T. Long, and X. Li, 2020. Sterols in an intramolecular channel of Smoothened mediate Hedgehog signaling. *Nat. Chem. Biol.* 16:1368–1375. doi:10.1038/s41589-020-0646-2.

7. Byrne, E. F. X., R. Sircar, P. S. Miller, G. Hedger, G. Luchetti, S. Nachtergaele, M. D. Tully, L. Mydock-McGrane, D. F. Covey, R. P. Rambo, M. S. P. Sansom, S. Newstead, R. Rohatgi, and C. Siebold, 2016. Structural basis of Smoothened regulation by its extracellular domains. *Nature* 535:517–522. doi:10.1038/nature18934.

8. Wang, C., H. Wu, T. Evron, E. Vardy, G. W. Han, X.-P. Huang, S. J. Hufeisen, T. J. Mangano, D. J. Urban, V. Katritch, V. Cherezov, M. G. Caron, B. L. Roth, and R. C. Stevens, 2014. Structural basis for Smoothened receptor modulation and chemoresistance to anticancer drugs. *Nat. Commun.* 5:4355. doi:10.1038/ncomms5355.